nature communications

Article

https://doi.org/10.1038/s41467-025-60207-4

Structural basis of ubiquitin ligase Nedd4-2 autoinhibition and regulation by calcium and 14-3-3 proteins

Received: 12 September 2024

Accepted: 19 May 2025

Published online: 26 May 2025

Check for updates

Masa Janosev[1], Dalibor Kosek[1], Andrej Tekel[1,2], Rohit Joshi[1,2], Karolina Honzejkova[2], Pavel Pohl[1], Tomas Obsil[1,2] ✉ & Veronika Obsilova[1] ✉

Nedd4-2 E3 ligase regulates Na^+ homeostasis by ubiquitinating various channels and membrane transporters, including the epithelial sodium channel ENaC. In turn, Nedd4-2 dysregulation leads to various conditions, including electrolytic imbalance, respiratory distress, hypertension, and kidney diseases. However, Nedd4-2 regulation remains mostly unclear. The present study aims at elucidating Nedd4-2 regulation by structurally characterizing Nedd4-2 and its complexes using several biophysical techniques. Our cryo-EM reconstruction shows that the C2 domain blocks the E2-binding surface of the HECT domain. This blockage, ubiquitin-binding exosite masking by the WW1 domain, catalytic C922 blockage and HECT domain stabilization provide the structural basis for Nedd4-2 autoinhibition. Furthermore, Ca^{2+}-dependent C2 membrane binding disrupts C2/HECT interactions, but not Ca^{2+} alone, whereas 14-3-3 protein binds to a flexible region of Nedd4-2 containing the WW2 and WW3 domains, thereby inhibiting its catalytic activity and membrane binding. Overall, our data provide key mechanistic insights into Nedd4-2 regulation toward fostering the development of strategies targeting Nedd4-2 function.

Ubiquitination is a posttranslational modification that determines the fate of proteins in cells through covalent attachment of ubiquitin (Ub). In addition to protein trafficking and degradation, cell survival, tumor suppression, and transcription involve ubiquitination[1]. This multistep process requires the coordinated and sequential activity of three enzymes. A Ub-activating E1 enzyme (E1) activates the Ub C-terminus and transfers activated Ub to a Ub-conjugating E2 enzyme (E2), which transfers thioester-linked Ub to an E3 ubiquitin ligase (E3), and E3 covalently attaches Ub to a protein for degradation[2].

In ubiquitin-mediated proteolysis, E3 ligases control selectivity by recognizing only target proteins with specific recognition signal[3]. Accordingly, the human genome encodes over 700 E3 ubiquitin ligases[4,5], classified into three families based on their catalytic domain, including the Homologous to the E6-AP Carboxyl Terminus (HECT) family[6]. Among its members, neural precursor cell expressed developmentally downregulated 4-like (Nedd4-2, also known as NEDD4L) stands out for its regulatory functions.

Nedd4-2 regulates multiple substrates, including various ion channels and transporters, maintaining cellular homeostasis primarily by downregulating the epithelial sodium channel (ENaC). Through its effect on ENaC, Nedd4-2 regulates Na^+ homeostasis and neuronal excitability[7]. Altered Nedd4-2 levels and single-nucleotide polymorphisms in the gene *NEDD4L* are associated with several types of cancer[8,9] and with hypertension and epilepsy[10,11], respectively. But while Nedd4-2 is a potential target for therapeutic intervention[12], efforts to develop effective treatments for these disorders have been hampered by our limited knowledge of the underlying mechanisms of Nedd4-2 regulation. Understanding

[1]Institute of Physiology of the Czech Academy of Sciences, Laboratory of Structural Biology of Signaling Proteins, Division BIOCEV, Prumyslova 595, 252 50 Vestec, Czech Republic. [2]Department of Physical and Macromolecular Chemistry, Faculty of Science, Charles University, Albertov 6, 128 43 Prague, Czech Republic. ✉e-mail: obsil@natur.cuni.cz; veronika.obsilova@fgu.cas.cz

Nedd4-2 regulation requires gaining further insights into its structure.

Nedd4 family has a unique modular multidomain architecture consisting of an N-terminal C2 domain, four WW domains (with a Pro and two conserved Trp residues), and a C-terminal catalytic HECT domain[8] (Fig. 1a). The HECT domain is a bi-lobed structure comprising an E2-binding N-terminal N-lobe and a C-terminal C-lobe with the catalytic cysteine residue. This C-lobe can move freely around a flexible hinge loop connected to the N-lobe in an L- or T-shaped arrangement[3]. The WW domains specifically recognize short Pro-rich motifs of target proteins (PPxY or LPxY, where x denotes any amino acid)[7]. These four WW domains have different functions and substrate specificity, which enable this enzyme to interact with numerous proteins[13]. Nedd4-2 also interacts with membranes because its C2 domain binds to membrane phospholipids in a Ca^{2+}-dependent manner[14]. In fact, the C2 domain is required for Ca^{2+}-dependent Nedd4-2 translocation to the membrane. The ability to form linkage-specific poly-Ub chains appears to be an intrinsic feature of HECT enzymes, as they are able to generate distinct Ub chains independently of the paired E2 enzymes. In general, members of the Nedd4 family specifically form K63-linked ubiquitin chains, at least in vitro[15]. Membrane binding markedly increases Nedd4-2 enzymatic activity[14,16] by disrupting interactions between the C2 and HECT domains, thereby stabilizing the active conformation of this enzyme[16]. As shown by NMR spectroscopy of isolated C2 and HECT domains, the C2 domain interacts with the HECT domain, Ca^{2+} ions, and inositol 1,4,5-trisphosphate through the same interface, indicating competition between these components[17]. Furthermore, three E3 ligases of the Nedd4 family, namely WWP1, WWP2, and Itch, adopt an inactive state characterized by intramolecular interactions, which block autoubiquitination and excessive target ubiquitination[18–22]. The main components of this autoinhibition are (1) the WW2 and WW4 domains, which interact with and mask surfaces of the HECT domain responsible for non-covalent Ub binding (Re site) and autoubiquitination (Le site), respectively and (2) the linker (L) region, which limits the flexibility of the HECT domain. The “re site” (Ub exosite) in the N-lobe of Nedd4-2 seems to be necessary for Nedd4-2 processivity by stabilizing and orienting the distal end of growing Ub chains on the substrate[23,24]. The “Le site” acts as a versatile regulatory site in the HECT domain to suppress Nedd4-2 activity[22]. These constrained conformational dynamics keep the HECT domain in an autoinhibited, inactive state, but many questions about the molecular mechanism of Nedd4-2 regulation are still unanswered. How exactly does C2 interact with the HECT and WW domains and contribute to Nedd4-2 autoinhibition? Do HECT interactions with WW domains and the regulatory linker region differ between Nedd4-2 and other Nedd4 E3 ligases? What is the role of other regulatory proteins?

Nedd4-2 is also regulated by 14-3-3 proteins, which recognize phosphorylated motifs adjacent to the WW2 domain in response to hormones, such as aldosterone, insulin or vasopressin[25–28]. 14-3-3 protein binding prevents Nedd4-2 from mediating ENaC ubiquitination[25], potentially through modulated interactions between structured domains of Nedd4-2 based on recent structural studies conducted with N-terminally truncated Nedd4-2 (lacking the C2 domain)[28,29]. However, the mechanism whereby 14-3-3 proteins inhibit Nedd4-2 remains unknown. Gaining further insights into Nedd4-2 regulation and into the role of Ca^{2+} and 14-3-3 binding in modulating Nedd4-2 activity requires an in-depth structural and functional analysis of this E3 ligase.

This study aims at characterizing the structure, catalytic activity, and membrane binding of full-length Nedd4-2 alone or in a complex with Ca^{2+} and 14-3-3 proteins. For this purpose, we use several biophysical methods, including cryo-electron microscopy (cryo-EM), small-angle X-ray scattering (SAXS), hydrogen/deuterium exchange coupled to mass spectrometry (HDX-MS), sedimentation velocity analytical ultracentrifugation (SV-AUC), and functional assays. Our cryo-EM reconstruction of full-length Nedd4-2 reveals that the C2 domain blocks the E2-binding surface of the HECT domain. Overall, Nedd4-2 uses a variation of the autoinhibition mechanism of other Nedd4 E3 ligases.

Results

Recombinantly expressed full-length Nedd4-2 is a catalytically active monomer

To gain structural insights into Nedd4-2 regulation, we recombinantly expressed and purified full-length Nedd4-2 isoform 5, also known as NEDD4Ld (UniProt ID Q96PU5-5). Compared to canonical isoform 1, Nedd4-2 isoform 5 lacks 20 residues in the region 356–375 and is expressed in most human tissues, albeit predominantly in the brain[30,31]. Purified Nedd4-2 was phosphorylated by PKA in vitro, and stoichiometric phosphorylation at both 14-3-3 binding motifs, S342 and S428, was confirmed by LC-MS analysis (Supplementary Fig. 1). Our experiments were performed with Nedd4-2 phosphorylated in this manner, unless stated otherwise, as one of our primary objectives was to examine the impact of phosphorylation-dependent 14-3-3 protein binding to Nedd4-2.

No significant differences were found in the catalytic activity of unphosphorylated and phosphorylated Nedd4-2 with and without Ca^{2+}, assessed using the fluorescence-based ubiquitination assay with the chloride transporter 5 (ClC-5) as a natural substrate and the autoubiquitination assay (Fig. 1b–d). The oligomeric state of unphosphorylated Nedd4-2 was characterized by sedimentation velocity analytical ultracentrifugation (SV-AUC). Without calcium, the sedimentation coefficient distribution *c(s)* showed a single peak with a 5.3 S weight-averaged sedimentation coefficient corrected to standard conditions of water density at 20.0 °C ($s_{w(20,w)}$) and a 1.43 frictional ratio (f/f_0) for ~ 96 kDa M_w, thus suggesting a monomeric state with a 110.5 kDa theoretical M_w under these conditions. In 1 mM $CaCl_2$, the results were similar, indicating that Ca^{2+} does not induce Nedd4-2 oligomerization (Fig. 1e).

Interdomain interactions restrict access to the active site and E2- and Ub-binding surfaces of the HECT domain

Cryo-EM imaging of full-length Nedd4-2 (with and without 1 mM $CaCl_2$) in buffer containing 3 mM CHAPSO revealed well-dispersed and uniform particles, as detailed in Methods, Supplementary Figs. 2, 3 and Supplementary Table 1. With 3.58 (without Ca^{2+}) and 4.11 (with Ca^{2+}) Å final resolution, the cryo-EM maps were highly similar, revealing the compact and asymmetric shape of Nedd4-2 (Fig. 1f and Supplementary Fig. 6a). Both maps enabled us to unambiguously place known crystal structure models of the C2 and HECT domains, along with WW1 and WW4 domains, based on the bulky sidechains (Fig. 2a and Supplementary Figs. 4a, 5, 6a), and to build the linker (L) region between WW1 and WW2 containing helix α1 (residues 233–251). The segment connecting C2 to WW1 and the part containing WW2 and WW3, including the 14-3-3 binding motifs, showed no density, presumably because they are highly flexible and/or unstructured.

The HECT domain of full-length Nedd4-2 displays a typical bi-lobal architecture and adopts a T-shaped conformation (Supplementary Fig. 8). This conformation mirrors those of autoinhibited Nedd4-family E3 ligases WWP1[22], WWP2[20], and Itch[21]. In comparison with the crystal structures of the Nedd4-2 HECT domain alone (PDB: 2ONI) and in a complex with E2 UbcH5B/Ub[32] (PDB: 3JVZ), the C-lobe is shifted and rotated, interacting with helices α10 and α15, in addition to the β23-β24 loop of the HECT N-lobe (Supplementary Fig. 6b, 7). The conformation of the HECT domain is stabilized by the helical L region, which interacts with both the hinge between the HECT N- and C-lobes and the ubiquitin-binding exosite and plays a key role in autoinhibition[20–22] (Fig. 2a and Supplementary Fig. 4a).

In the Nedd4-2 structure, large interdomain interfaces separate the C2/HECT, HECT/WW1, HECT/L, and HECT/WW4 domains (Fig. 2a).

https://doi.org/10.1038/s41467-025-60207-4

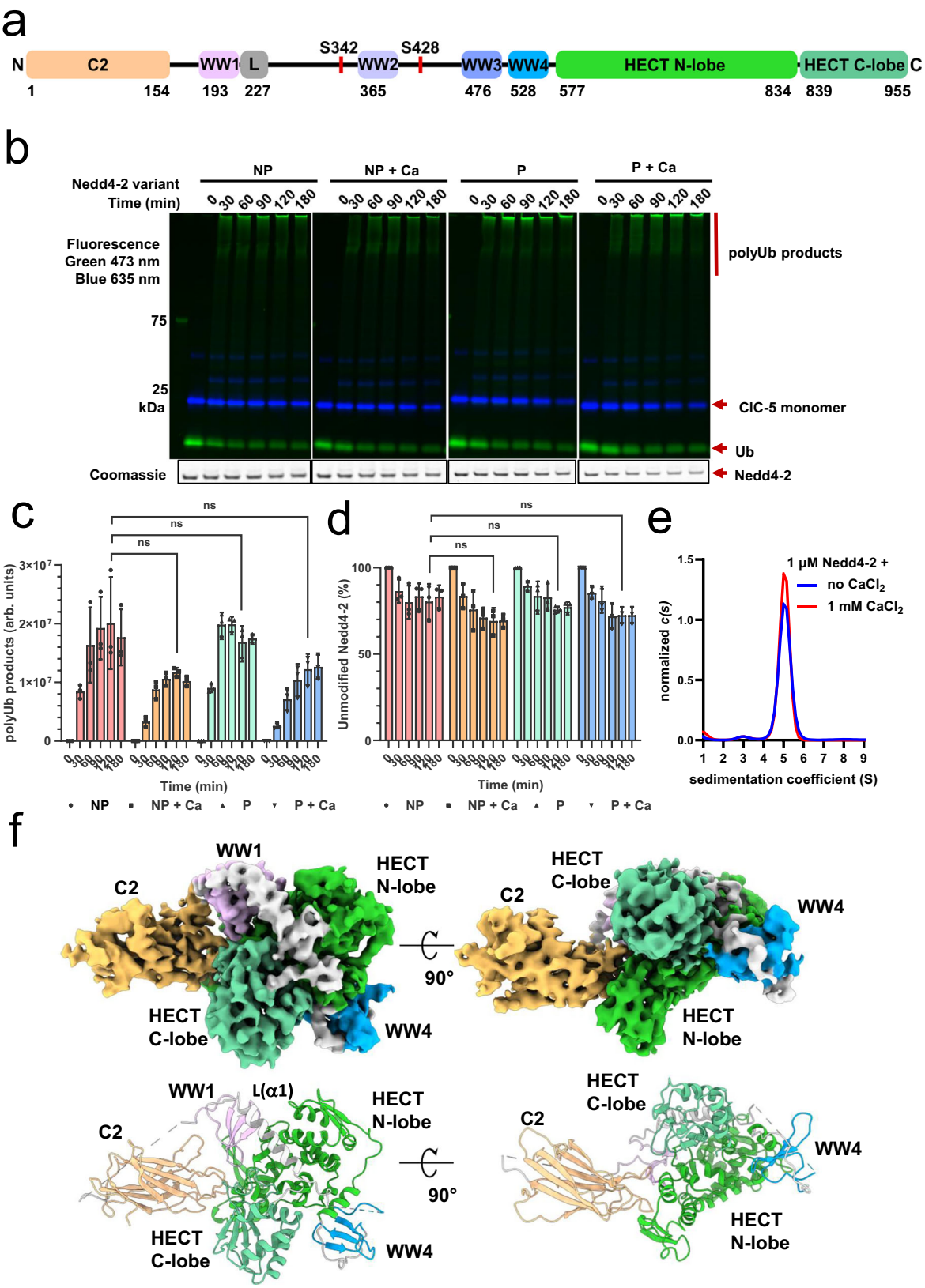

C2 interacts with helix α11 of the HECT N-lobe and with loop β9-β10 in WW1 via loops β1-β2 (residues 36-38), β3-β4 (residue 68), and β5-β6 (residues 98–101). When comparing the cryo-EM structure of Nedd4-2 with the crystal structure of the Nedd4-2 HECT domain in a complex with E2 UbcH5B covalently bound to Ub[32], we found that the C2 binding site overlaps with the E2-binding surface (Supplementary Fig. 6b). The WW1 domain is embedded in a groove at the interface between C2 and HECT close to the α5-α7 loop of the HECT N-lobe (Supplementary Fig. 6c). This α5-α7 loop is the ubiquitin-binding exosite for non-covalently bound ubiquitin (Re site) identified in previous studies[22,24,33,34]. As in the structure of the HECT E3 ligase WWP1[22], the second WW4 domain interacts with the Le site at the opposite side

Fig. 1 | Characterization of full-length Nedd4-2 in solution. a Schematic representation of the domain structure of Nedd4-2 isoform 5. C2, calcium binding domain (peach); WW1 (pale purple); L region (gray); WW2 (pale blue); WW3 (cornflower blue); WW4 (blue); HECT N-lobe, N-lobe of the catalytic HECT domain (light green); HECT C-lobe, C-lobe of the catalytic HECT domain (forest green). Red lines denote the phosphorylation sites/14-3-3-binding motifs S342 and S428. **b** Analysis of Nedd4-2-mediated ubiquitination of the chloride channel ClC-5 under four experimental conditions: NP unphosphorylated, P phosphorylated, and with or without 1 mM $CaCl_2$. Proteins were separated on a 4–15% SDS-PAGE polyacrylamide gradient gel and visualized by in-gel fluorescent imaging: fluorescein-labeled ubiquitin (green, 473 nm) and AF633-labeled ClC-5 (blue, 633 nm). A Coomassie blue-stained gel showing the unmodified Nedd4-2 is shown below. **c** Quantification of ubiquitinated products by in-gel fluorescent imaging at 473 nm (arb. units arbitrary units). **d** Quantification of unmodified Nedd4-2 from Coomassie blue-stained SDS-PAGE gels. The intensities at each time point (**c**, **d**) were normalized to the intensity at time zero. Data represent mean ± SD from three independent experiments. Statistical significance was determined using an unpaired two-tailed Student's *t*-test (ns non-significant $p > 0.05$). **e** Area-normalized distribution of sedimentation coefficients ($c(s)$) of unphosphorylated Nedd4-2 in a buffer with (red) and without (blue) 1 mM $CaCl_2$. **f** Cryo-EM density map generated using threshold level 7 with a cartoon representation of the Nedd4-2 model, L(α1), α1 helix in the L region. Source data are provided as a Source Data file.

of the HECT N-lobe formed by helices α2 and α14. This N-lobe contains the autoubiquitination site K580 (Fig. 2a and Supplementary Fig. 8b).

Unlike the L region of WWP1/2 and Itch, which is located after the WW2 domain and adopts a bent conformation, the L region of Nedd4-2 directly follows the WW1 domain (Supplementary Fig. 8a), and its α1 helix is shorter and straight. As a result, the N-terminal section of this L region occupies a different position, likely because the WW1 domain is bound to the Re site at the interface between C2 and the N-lobe of HECT (Fig. 2a and Supplementary Figs. 8b–d, 9a). Consequently, the L region of Nedd4-2 interacts with the HECT domain only through its C-terminal section via residues Q242, R247, R248, F249, R252, and R253 (Fig. 2a). Given its proximity to helices α10 and α11 of the HECT N-lobe and to the binding interface between the HECT and C2 domains, the catalytic residue C922 cannot be accessed in Nedd4-2 (Fig. 2a).

The C2 domain loops that interact with the HECT and WW1 domains contain six conserved residues, namely D36, D42, D95, N97, D102 and D103, which coordinate two Ca^{2+} ions[35] (Fig. 2a). When superimposing the cryo-EM structure of the Nedd4-2 C2 domain on available crystal structures of Nedd4-2 and Nedd4-1 isoform 4 C2 domains (PDB: 2NSQ and 3B7Y), we noted that the Ca^{2+}-binding loops had a different conformation in the cryo-EM structure, possibly due to interactions with the HECT N-lobe (Supplementary Fig. 9b, c). Furthermore, we were unable to find any 3D class during the processing of cryo-EM data collected on Nedd4-2 that would contain additional density for Ca^{2+} ions even in the presence of 1 mM $CaCl_2$ (Supplementary Fig. 4b). Combined, these data suggest very low occupancy of Ca^{2+}-binding sites in full-length Nedd4-2.

To further analyse the observed interactions and their importance in autoinhibition of Nedd4-2, four mutant variants were designed based on the cryo-EM structure. The variant M1 contained mutations R98A + T100A + R101A at the interface between the C2 and HECT domains; the variant M2, mutations N205A + R208A + H214A at the interface between the WW1, C2 and HECT domains; the variant M3 mutations R537A + H549A + K552A at the interface between WW4 and HECT domains; and the variant M4, mutations R98A + T100A + R101A + N205A + R208A + H214A combining mutations from M1 and M2. The autoubiquitination assay revealed that Nedd4-2 variants M1, M2, and M4 (WW1-C2-HECT interface) showed significantly increased autoubiquitination activity, specifically by more than 75% after 2 h of incubation. A less prominent (50%) increase was observed for the M3 variant with mutations at the WW4-HECT interface (Fig. 2b). In addition, significantly increased activity of all four mutant variants of Nedd4-2 is also evident from the results of fluorescence-based autoubiquitination assay (Supplementary Fig. 10a, b). These results thus confirm the role of interdomain interactions in the autoinhibition of Nedd4-2.

Nedd4-2 does not undergo large calcium-induced structural alterations in the absence of a lipid membrane

The absence of major structural changes with Ca^{2+} was confirmed by size-exclusion chromatography (SEC) coupled to small-angle X-ray scattering (SAXS) (Supplementary Fig. 11a–d). Our model-independent analysis of SAXS data showed that Nedd4-2 has apparent molecular weights of 131 and 119 kDa with and without 1 mM Ca^{2+}, respectively (Supplementary Table 2), as expected based on the protein sequence (110.5 kDa M_w). From scattering data collected with and without Ca^{2+}, we calculated similar values of radius of gyration (R_g) and maximum distance (D_{max}), suggesting that Ca^{2+} has no major effect on the overall conformation of Nedd4-2. In addition, the distance distribution functions $P(r)$ and the dimensionless Kratky plots ($(sR_g)^2I(s)/I_0$ versus sR_g), where s is the momentum transfer, $I(s)$ is the scattering intensity, and I_0 is the extrapolated intensity at zero angle) were also highly similar. These findings support our assertion that calcium binding to Nedd4-2 does not induce large changes in conformation or flexibility (Supplementary Fig. 11e, f).

Our SAXS data complemented the cryo-EM structure and enabled us to build a complete structural model of Nedd4-2, including the missing domains in the cryo-EM reconstruction. The best-scoring CORAL[36] model of Nedd4-2 fit the experimental SAXS data with a χ^2 of 1.55. This model indicates that the segment with the WW2 and WW3 domains and the 14-3-3 binding motifs is highly flexible, adopting an extended conformation with minimal contact with the "rigid" section formed by the C2, HECT, WW1, and WW4 domains (Supplementary Fig. 12).

We further analyzed interactions between Ca^{2+} and Nedd4-2 by HDX-MS. HDX-MS monitors the kinetics of backbone amide hydrogen exchange, which depends on solvent exposure and hydrogen bonding. Flexible or solvent-exposed regions are rapidly deuterated, in contrast to buried regions and those involved in the formation of stable secondary structure elements or hydrogen bonds.

With 1 mM Ca^{2+}, several Nedd4-2 regions showed significantly higher deuterium uptake, deprotection (Fig. 3a, b and Supplementary Figs. 13, 14), especially after a 20-s-long deuteration in the loops β1-β2 and β5-β6 (residues 32–50 and 95–98) of the Ca^{2+}-binding C2 domain (Figs. 2a, 3 and Supplementary Figs. 9b, c). Significant deprotection was also observed after a 1200-s-long deuteration in other segments, namely 132–149 in the C2 domain, 249–277 between WW1 and WW2, 401–433 between WW2 and WW3, 516–526 in the WW4 domain and 583–601, 666–669, and 730–736 in the HECT N-lobe. These regions include interfaces between the HECT N-lobe and the C2 domain, between the HECT domain and the L region, and between the HECT N-lobe and the WW4 domain (Fig. 3b).

In these regions, increased deuterium uptake implies transient Ca^{2+} binding to the C2 domain, which may disrupt interactions between the C2 and HECT domains. The high deuteration levels of segments located between WW domains (Fig. 3 and Supplementary Fig. 14) are also in line with their high flexibility, as suggested by the cryo-EM model. Notwithstanding transient Ca^{2+} binding, our cryo-EM reconstruction and SAXS data indicate that Nedd4-2 does not undergo any quantitative calcium-induced structural alterations in the absence of a lipid membrane.

Nedd4-2 undergoes structural reorganization upon membrane binding

Previous studies have suggested that Nedd4-2 binds to the membrane in a Ca^{2+}-dependent manner through its C2 domain[14,16]. In this study, we

https://doi.org/10.1038/s41467-025-60207-4

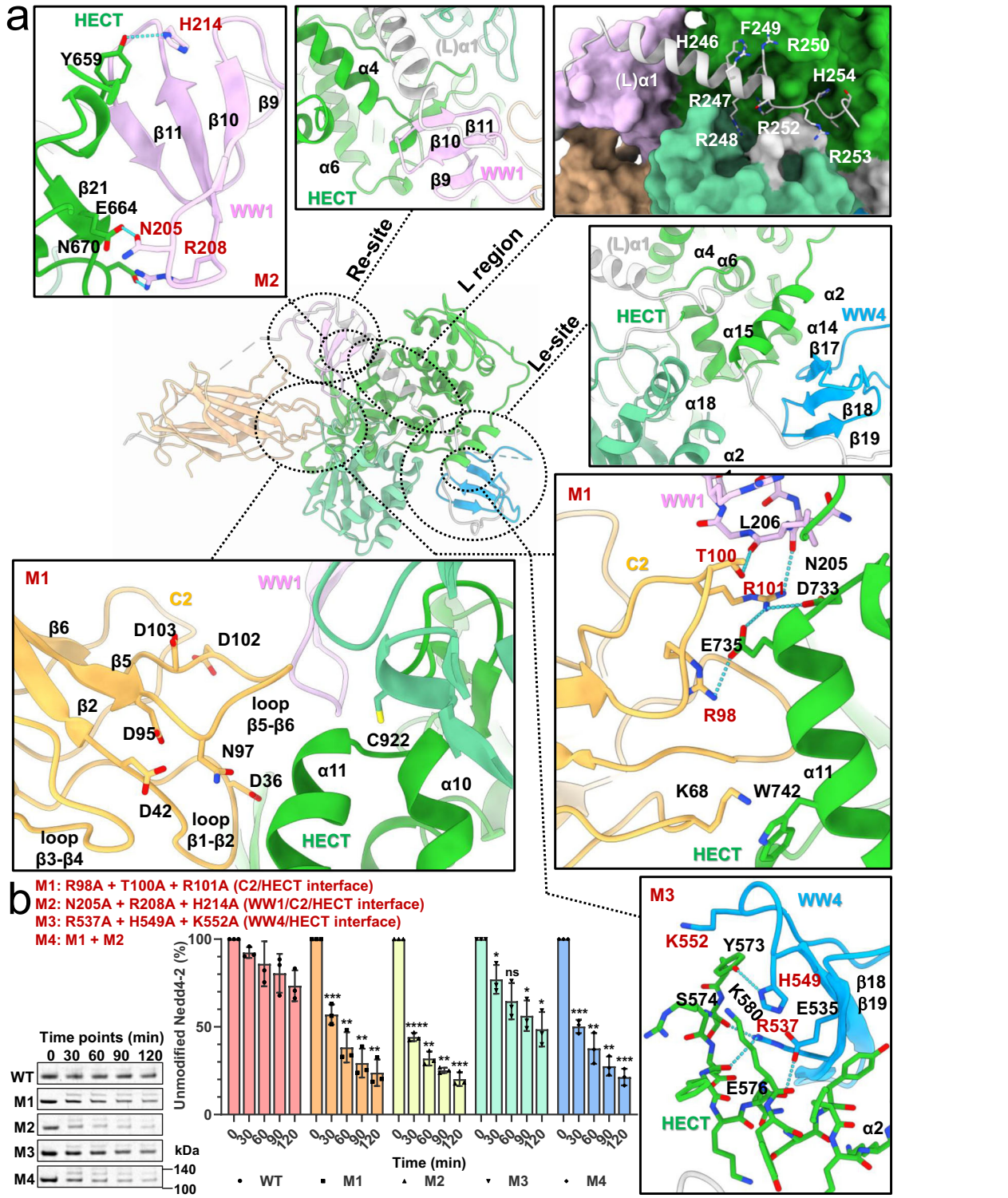

Fig. 2 | Cryo-EM structure of full-length Nedd4-2. a Cartoon representation of the Nedd4-2 model from cryo-EM reconstruction with close-up views of the interface regions between C2 (in peach), WW1 (in pale purple), WW4 (in blue), and HECT (in green) domains. Sidechains of important residues are indicated in sticks and labeled. Teal dashed lines indicate atom-atom distances within H-bonding range. Position of the α1 helix in the L region. Re site and Le site are marked in the figure. Mutated residues are labeled in red. **b** Autoubiquitination assay of Nedd4-2 and its mutant variants on the interfaces of individual domains. Proteins were separated on a 4–15% polyacrylamide gradient gel using SDS-PAGE. WT wild-type, M1–M4 the mutant variants. Unmodified Nedd4-2 was quantified and normalized to the zero time point. Data represent mean ± SD from three independent experiments. Statistical significance was determined using an unpaired two-tailed Student's *t*-test (ns non-significant $p > 0.05$; *$p \le 0.05$; **$p \le 0.01$; ***$p \le 0.001$; ****$p \le 0.0001$). Source data are provided as a Source Data file.

https://doi.org/10.1038/s41467-025-60207-4

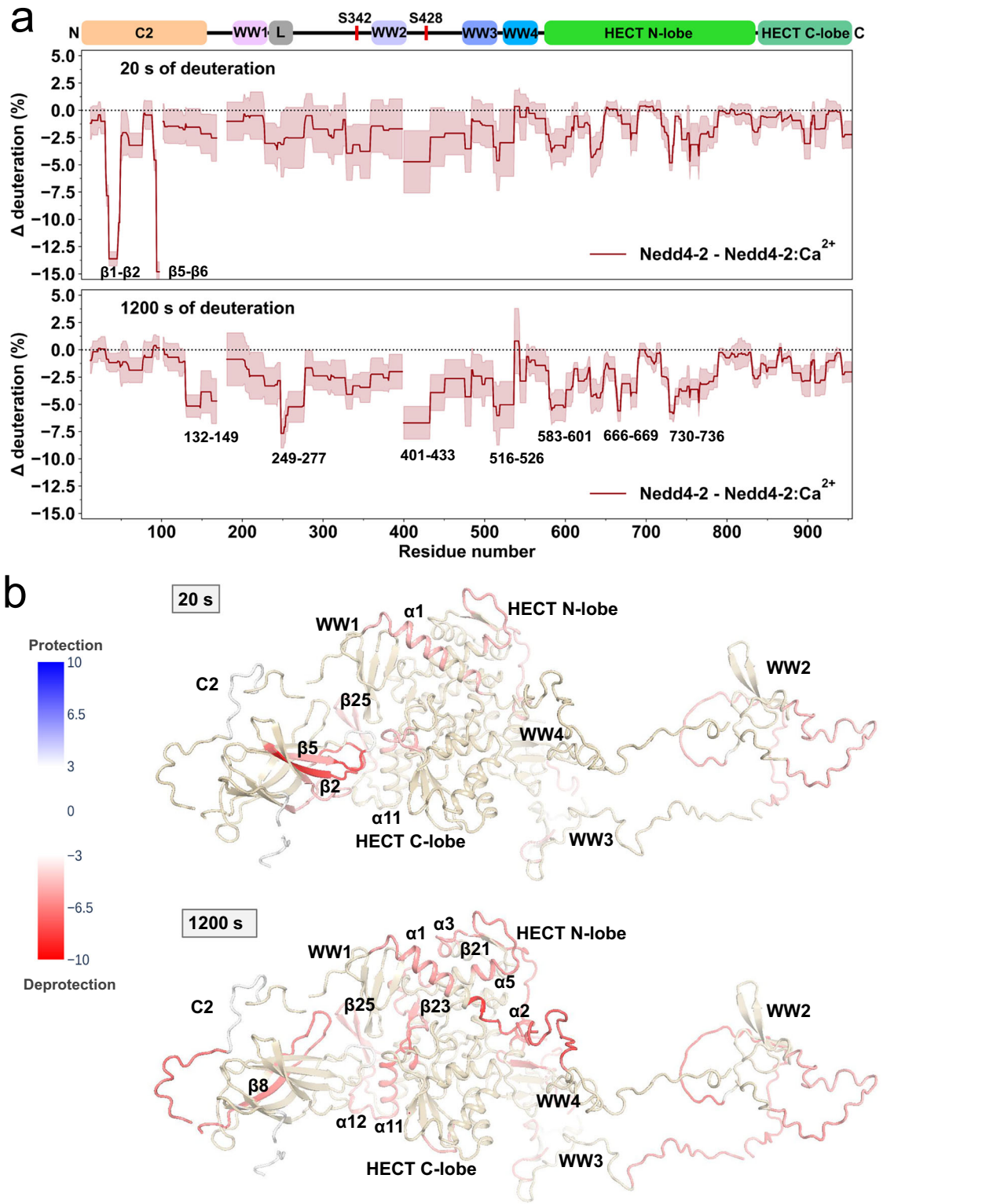

Fig. 3 | Calcium does not induce large conformational changes in Nedd4-2. **a** Differential effects of calcium on deuterium uptake of Nedd4-2 after 20 and 1200 s of deuteration. The plotted data represent the difference in deuteration with and without 1 mM Ca^{2+}. Negative values depict Nedd4-2 regions with increased deuterium uptake (deprotection) without Ca^{2+}. Light red shade indicates mean ± SD of three technical replicates. Breaks within plots result from missing data (regions without coverage). Significant changes are marked with residue numbers. The domain structure of Nedd4-2 is shown at the top. C2 calcium binding domain, WW1-4 WW domains, L L region, HECT N-lobe N-lobe of the catalytic HECT domain, HECT C-lobe C-lobe of the catalytic HECT domain. **b** HDX-MS differences mapped on the SAXS-based model of full-length Nedd4-2. Deprotected and protected regions are indicated in red and blue, respectively, in the presence of Ca^{2+}. Source data are provided as a Source Data file.

https://doi.org/10.1038/s41467-025-60207-4

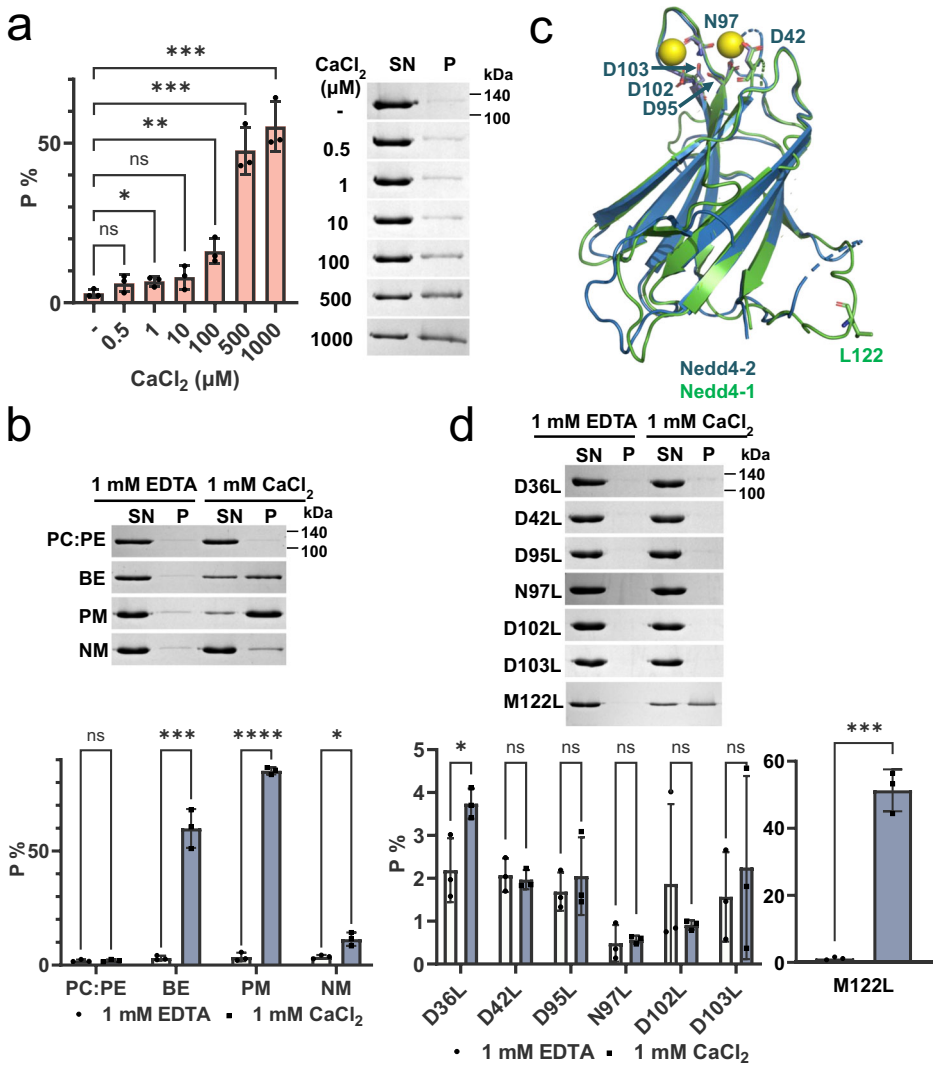

Fig. 4 | Nedd4-2 binds to the lipid membrane via the N-terminal C2 domain in a Ca^{2+}-dependent manner. a Nedd4-2 binding to BE-based LUVs with different concentrations of Ca^{2+}. **b** Nedd4-2 binding to LUVs with different compositions. SN, supernatant; P, pellet (lipid-bound fraction); PC:PE, in 80:20 ratio; BE, Brain Polar Extract; PM, plasma-mimicking membrane; NM, nuclear-mimicking membrane. **c** Comparison of the crystal structure of the Nedd4-1 C2 domain bound to Ca^{2+} (PDB: 3B7Y) with the crystal structure of the Nedd4-2 C2 domain without Ca^{2+} (PDB: 2NSQ). The residues involved in calcium binding are labeled and shown as sticks. The position of the residue L122 of Nedd4-1, corresponding to M122 in Nedd4-2, which was used as a negative control (Nedd4-2 M122L mutation), is labeled and highlighted in green (primary sequence alignment of these domains is shown in Supplementary Fig. 15a). **d** Mutant Nedd4-2 binding to BE-based LUVs with and without 1 mM Ca^{2+}. Quantified data (**a**, **b**, **d**) are expressed as means ± SD of three independent experiments. Statistical significance was determined using an unpaired two-tailed Student's *t*-test (ns, non-significant $p > 0.05$; *$p \le 0.05$; **$p \le 0.01$; ***$p \le 0.001$; ****$p \le 0.0001$). P% represents the percentage of protein in the pellet relative to the sum of densities of both supernatant and pellet fractions (P/(SN + P)). Source data are provided as a Source Data file.

confirmed that Nedd4-2 binds to the membrane in a Ca^{2+}-dependent manner through liposome-binding assays using large unilamellar vesicles (LUVs) prepared from porcine brain polar lipid extract (BE) to mimic the physiological lipid composition of brain cells (Fig. 4a, b). Significant (50–60% membrane-bound fraction (MF)) Nedd4-2 binding to BE-based LUVs was observed with at least 0.5 mM $CaCl_2$.

In addition to BE-based LUVs, we tested three other LUVs for Nedd4-2 binding. Nedd4-2 binding to plasma membrane (PM)-mimicking LUVs was efficient (82 ± 1% MF). Conversely, Nedd4-2 binding to nuclear membrane (NM)-mimicking LUVs was weak (8 ± 2% MF), with no binding in the negative control (80:20 1-palmitoyl-2-oleoyl-*sn*-glycero-3-phosphocholine:1-palmitoyl-2-oleoyl-*sn*-glycero-3-phosphoethanolamine (PC:PE)) containing LUVs (Fig. 4b). As expected, removing the N-terminal C2 domain abrogated Nedd4-2ΔN binding to BE-based LUVs. Alone, the C2 domain showed efficient membrane binding (79 ± 3% MF) (Supplementary Fig. 15b). Similarly, unphosphorylated Nedd4-2 binds to BE and PC:PE membranes as to phosphorylated Nedd4-2 (Supplementary Fig. 15a). To rule out calcium-induced liposome aggregation, which would affect the results of the liposome-binding assay, we also compared the size distributions of BE-based LUVs with and without various calcium concentrations using multi-angle dynamic light scattering (MADLS). These measurements showed that calcium does not cause aggregation of BE-based LUVs, because the same monodisperse particle size distribution was obtained in all cases (Supplementary Fig. 15c).

The C2 domain of Nedd4-2 contains two conserved Ca^{2+}-binding sites (Figs. 2a, 4c and Supplementary Figs. 9c, 16a). To assess whether both sites are required for Nedd4-2 membrane binding, we replaced these residues and M122 (control) with leucine by site-directed mutagenesis and examined the structural integrity of the mutants by Differential scanning fluorimetry (DSF) and circular dichroism (CD) spectroscopy. DSF revealed that D42L, D95L, and D102L Nedd4-2

mutants had a slightly lower melting temperature (T_m), whereas the other mutations did not cause any significant shift in T_m (Supplementary Fig. 16b–d). Far-UV CD analysis showed no significant difference in secondary structure between Nedd4-2 WT and all mutants, with ~23% α-helix, ~26% β-sheet (16% antiparallel and 10% parallel), ~18% β-turn, and ~33% random coil. The combined DSF and CD data suggest that none of the mutations significantly affected Nedd4-2 stability. Nevertheless, in liposome-binding assays with Nedd4-2 mutants and BE-based LUVs, all mutations, except the control M122L, prevented Nedd4-2 binding to LUVs (Fig. 4d). Therefore, both Ca^{2+}-binding sites in the C2 domain should be required for Nedd4-2 binding to the membrane.

Nedd4-2 interactions with the lipid membrane were subsequently studied by HDX-MS. When comparing the deuteration profiles of Nedd4-2:Ca^{2+} with and without BE-based LUVs, we found significant higher deuterium uptake (deprotection) in C2 domain regions including residues 50–57 (the β2-β3 loop), 78–91 (strands β4 and β5), 92–98 (the β5-β6 loop involved in Ca^{2+} binding), interfaces between the C2 domain and the N- and C-lobes of the HECT domain (residues 131–148, 182–227, and 645–648), and the hinge region (residues 825–842) (Fig. 5a and Supplementary Figs. 17, 18). These results suggest that membrane binding presumably induces a conformational rearrangement, which relieves interactions in the "locked", autoinhibited conformation of Nedd4-2 (Fig. 2a) and increases the flexibility and/or solvent accessibility of many regions.

In contrast, deuterium uptake was significant lower in (1) four regions of the C2 domain (residues 32–49, 109–116, and 123–127) including the β1-β2 loop involved in calcium binding, (2) the WW2 domain, and (3) five regions of the HECT domain (including the helix α2, which interacts with WW4) (Fig. 5b). Hydrophobicity analysis of Nedd4-2 sequence[37] revealed that four of these regions are surface-exposed hydrophobic patches (Supplementary Fig. 19, segments labeled in red). These protected and hydrophobic segments are likely the Nedd4-2 membrane binding sites. Alternatively, protection may also reflect interactions between these segments and other Nedd4-2 regions and/or conformational changes induced by membrane binding.

We also compared the deuteration profiles of N-terminally truncated Nedd4-2ΔN lacking the C2 domain in the presence of Ca^{2+} and with and without BE-based LUVs. No significant differences were observed between the two samples. This result confirms that Nedd4-2 membrane binding is driven by its C2 domain (Supplementary Fig. 20).

14-3-3 protein binding reduces Nedd4-2 catalytic activity and membrane binding

14-3-3 proteins recognize two phosphorylated motifs (S342 and S428) bordering the WW2 domain (Fig. 1a) and, as such, are key Nedd4-2 interactors and regulators[25,26,28,29]. In our previous study with the N-terminally truncated Nedd4-2, without the C2 domain, we showed that 14-3-3η binding induces a conformational rearrangement of Nedd4-2 by inhibiting interactions between its structured domains[28,29]. However, the presence of the C2 domain and the stabilization of the autoinhibited locked conformation may have a significant effect on the interaction of full-length Nedd4-2 with 14-3-3. In addition, Nedd4-2 membrane binding affects deuterium uptake in regions containing 14-3-3 binding motifs (Fig. 5a). Therefore, we assessed the effect of 14-3-3η binding to Nedd4-2 on its ability to associate with the membrane.

To this end, we first characterized the interaction between Nedd4-2 and 14-3-3η by size-exclusion chromatography (SEC). Comparison of elution profiles of Nedd4-2 alone, 14-3-3η alone and their mixture (1:2 molar ratio) confirmed the formation of the complex (Supplementary Fig. 21). Subsequently, we assessed the stability of the Nedd4-2:14-3-3η complex by SV-AUC analysis of its mixtures at various molar ratios ranging from 5:1 to 1:20 (Fig. 6a, b). Based on *c(s)*, Nedd4-2 and 14-3-3η formed a complex with 7.0 S $s_{w(20,w)}$ and 1.40 f/f_O, which corresponds to ~142 kDa M_w and to 1:2 M stoichiometry (167.3 kDa theoretical M_w). Using the Lamm equation, we directly modeled SV-AUC data, which showed best-fit apparent equilibrium dissociation constants (K_D) of 3 nM (confidence interval <13 nM), with one Nedd4-2 molecule interacting with a 14-3-3η homodimer. Titration with 1 mM $CaCl_2$ indicated a similar binding affinity, with a K_D of 8 nM (3–17 nM confidence interval), nearly matching the titration without Ca^{2+}.

In the autoubiquitination assay, 14-3-3η in a 2 and 5 molar excess decreased autoubiquitination by ~20 and 40% (Fig. 6c, d), respectively, in line with previously published data on N-terminally truncated Nedd4-2 without the C2 domain[28]. The control experiment with unphosphorylated Nedd4-2, which is unable to bind 14-3-3, showed no significant changes in autoubiquitination (Supplementary Fig. 22a, b). However, in liposome competitive binding assays, 14-3-3η inhibited Nedd4-2 binding to BE-based LUVs in a concentration-dependent manner, decreasing the Nedd4-2 MF by approximately one-third in a twofold molar excess and by approximately half in a five- and tenfold excess (Fig. 6e). In contrast, unphosphorylated Nedd4-2 binding to BE-based LUVs was considerably less affected by the presence of 14-3-3η, as a significant decrease in the Nedd4-2 MF was observed only at the highest concentration of 14-3-3η (tenfold excess) (Supplementary Fig. 22c). Taken together, these results demonstrate that 14-3-3 protein binding reduces Nedd4-2 catalytic activity and membrane binding.

To better understand the inhibitory effect of 14-3-3η on Nedd4-2 catalytic activity and membrane binding, we performed HDX-MS measurements. The comparison of Nedd4-2 deuteration profiles with and without 14-3-3η in the absence of BE-based LUVs revealed significant 14-3-3η-mediated protection only in two Nedd4-2 regions (Supplementary Fig. 23), namely the segment between WW2 and the 14-3-3 binding motif S428, which is the dominant high-affinity binding site[28], and the 485-501 segment of WW3, which may directly interact with 14-3-3η[28]. Given the absence of major changes in deuterium uptake, 14-3-3η binding should not induce large structural changes in full-length Nedd4-2 despite interacting with 14-3-3 binding motifs and WW3. HDX-MS measurements in the presence of BE-based LUVs revealed similar but not identical changes in the deuteration of Nedd4-2 alone and in a complex with 14-3-3η (Fig. 5 and Supplementary Fig. 24). These similar deuteration profiles suggest that most Nedd4-2 remain bounded to the membrane under the given conditions (twofold molar excess of 14-3-3η).

The deuteration profiles of Nedd4-2:Ca^{2+}:LUV and Nedd4-2:Ca^{2+}:14-3-3η:LUV, conversely, revealed both lower deuteration in the WW1-L and WW2-WW3 regions and changes in the deuteration of several regions of the HECT domain in the presence of 14-3-3η (Supplementary Fig. 25). These differences are most likely related to the direct effect of 14-3-3η on the structure of Nedd4-2 and to the weaker interaction of the Nedd4-2:Ca^{2+}:14-3-3η complex with the membrane. As a result, a fraction of Nedd4-2 molecules remain in the autoinhibited state, as indicated by the protection in the WW1-L region and in regions 577–583 (the Le site at the HECT/WW4 interface) and 665–670 (the interface between N- and C-lobes of the HECT domain near the Re site). Therefore, 14-3-3η may inhibit Nedd4-2 membrane binding by interfering with the flexible region containing the 14-3-3 binding motifs and WW2, whose deuterium uptake is affected by both 14-3-3η (Supplementary Fig. 23) and LUVs (Fig. 5). The decrease in catalytic activity likely derives not only from reduced activation of Nedd4-2 in the presence of 14-3-3η but also from reduced WW2 and WW3 accessibility and/or transient interactions with HECT, as suggested by our previous studies[28,29].

Only in helices H3 and H9 did we find significant protection when comparing deuteration profiles of 14-3-3η with and without Nedd4-2 (Supplementary Figs. 26, 27). These helices form the walls of the ligand-binding groove of the 14-3-3 protein and contain residues responsible for binding to phosphorylated motifs. In addition, the outside surface of the helix H9 frequently contributes to interactions with 14-3-3 protein-binding partners[38]. These data suggest that 14-3-3η

https://doi.org/10.1038/s41467-025-60207-4

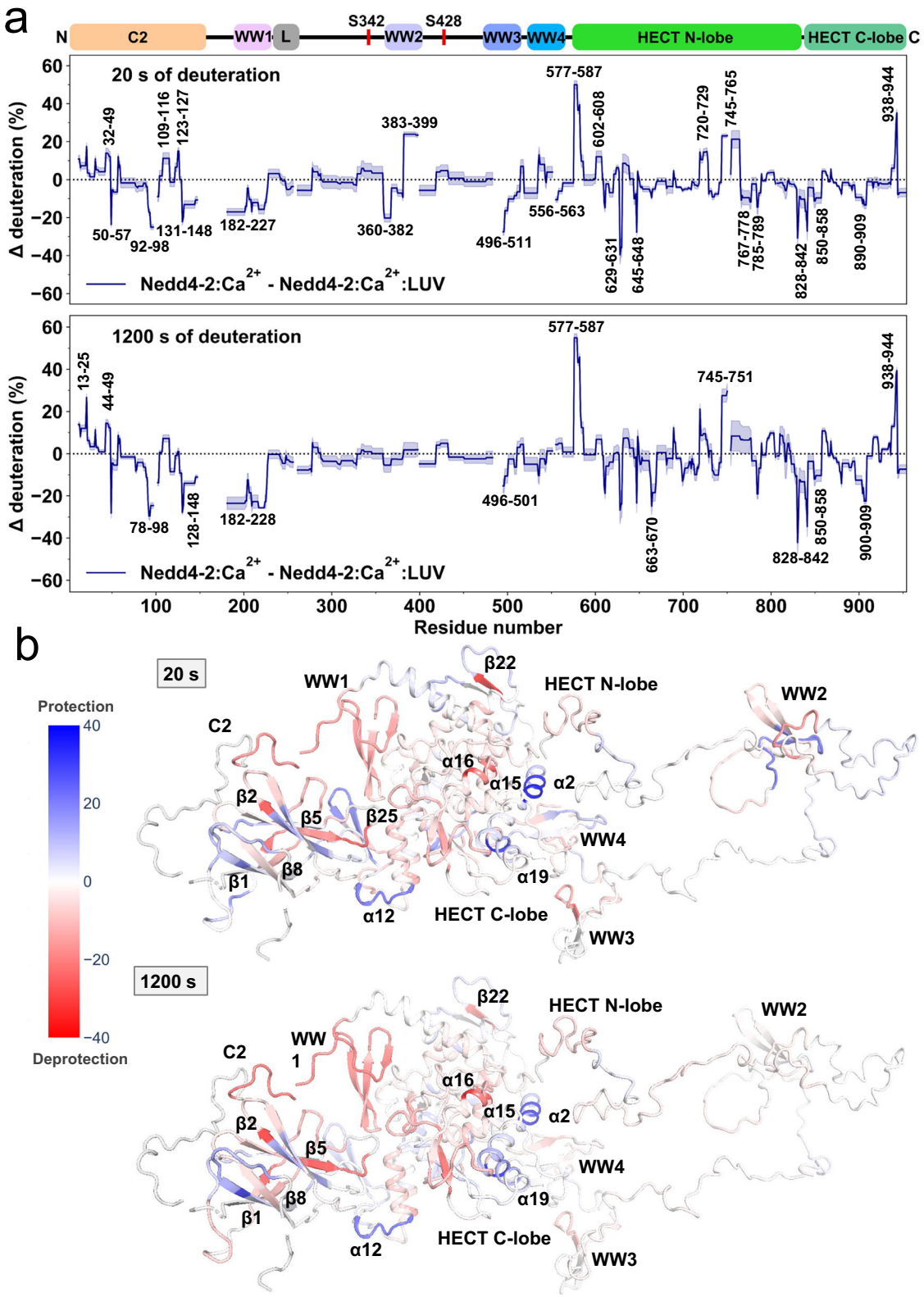

Fig. 5 | Nedd4-2 undergoes structural reorganization upon membrane binding. **a** Differential effects of LUVs on deuterium uptake of Nedd4-2 with 1 mM Ca^{2+} after 20 and 1200 s of deuteration. The plotted data represent the difference in deuteration with and without BE-based LUVs. Positive and negative values indicate Nedd4-2 regions with decreased (protection) and increased (deprotection) deuterium uptake in the presence of LUVs, respectively. Light blue shade indicates mean ± SD of three technical replicates. Breaks in plots result from missing data (regions without coverage). Nedd4-2 segments with significant changes are marked with residue numbers. The domain structure of Nedd4-2 is shown at the top. C2 calcium binding domain, WW1-4 WW domains, HECT N-lobe N-lobe of the catalytic HECT domain, HECT C-lobe C-lobe of the catalytic HECT domain. **b** HDX-MS differences mapped on a SAXS-based model of full-length Nedd4-2. Deprotected and protected regions in the presence of LUVs are indicated in red and blue, respectively. Source data are provided as a Source Data file.

https://doi.org/10.1038/s41467-025-60207-4

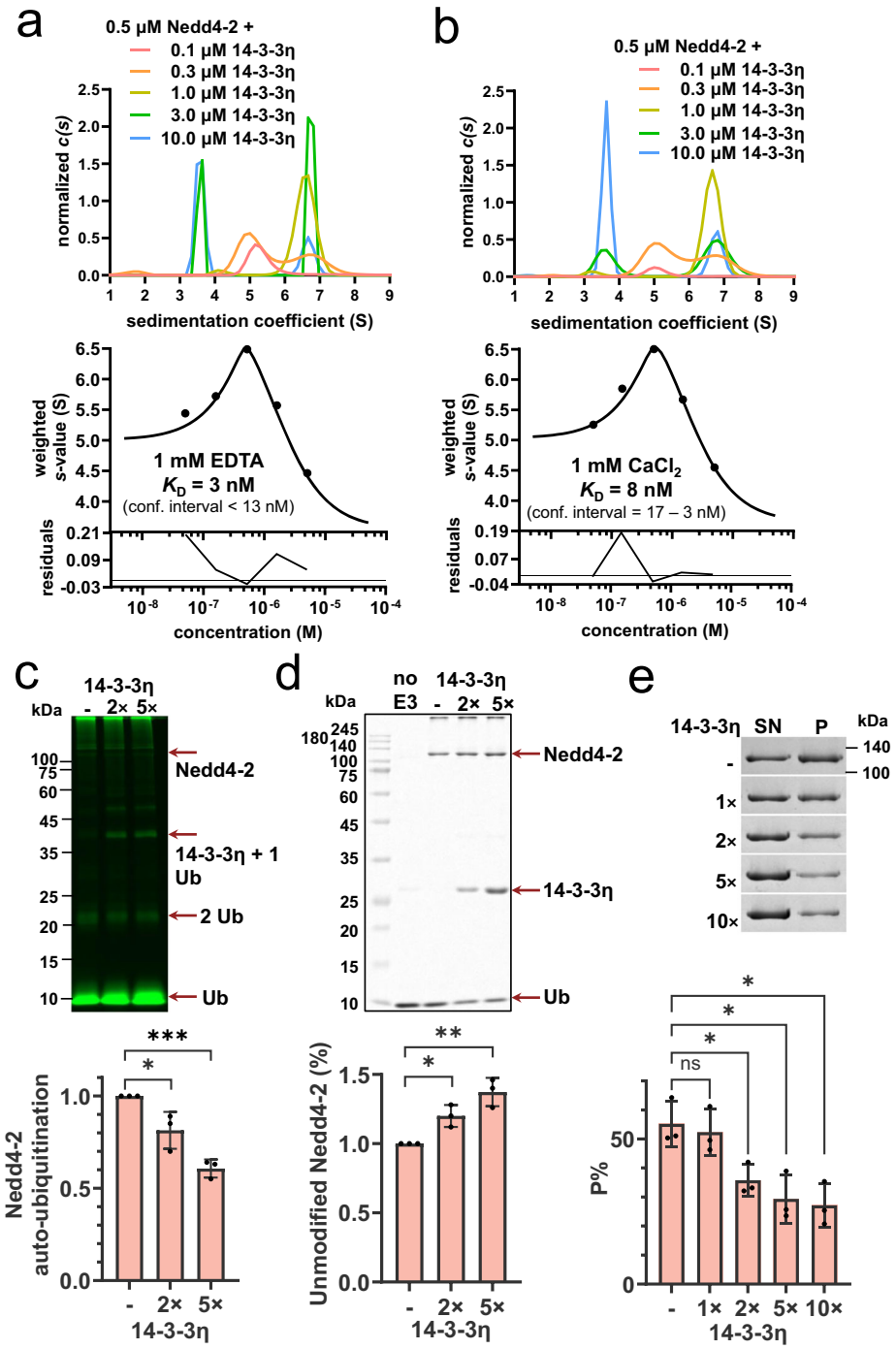

Fig. 6 | 14-3-3 protein blocks Nedd4-2 membrane binding and catalytic activity. **a**, **b** Series of area-normalized sedimentation coefficient distributions $c(s)$ of Nedd4-2 and 14-3-3η mixtures at various molar ratios, using 0.5 µM Nedd4-2 and 0.1–10 µM 14-3-3η. The binding curve of weight-average sedimentation coefficients s_w was calculated from SV-AUC experiments with 14-3-3η and Nedd4-2 mixtures in buffer containing 1 mM EDTA (**a**) or 1 mM Ca^{2+} (**b**). **c** Autoubiquitination reaction results after 60 min of incubation without 14-3-3η (-) and with a 2× or 5× molar excess of 14-3-3η. Ubiquitinated products were visualized and quantified by in-gel fluorescent imaging using fluorescein-labeled ubiquitin (green, excitation at 473 nm). Intensities were normalized to the sample without 14-3-3η. **d** Quantification of unmodified Nedd4-2 after a 60-min autoubiquitination reaction was performed without 14-3-3η (-) and with a 2× or 5× molar excess of 14-3-3η. Unmodified Nedd4-2 was quantified from Coomassie blue-stained SDS-PAGE gels and normalized to the reaction lacking 14-3-3η. **e** Nedd4-2 binding to BE-based LUVs with 1 mM Ca^{2+} and various molar excesses of 14-3-3η. P%, percentage of protein in the pellet, relative to the sum of densities of both supernatant and pellet fractions (P/(SN + P)). Quantified data (**c**–**e**) are expressed as means ± SD of three independent experiments. Statistical significance was determined using an unpaired two-tailed Student's t-test (ns, non-significant $p > 0.05$; $^{*}p \le 0.05$; $^{**}p \le 0.01$; $^{***}p \le 0.001$). Source data are provided as a Source Data file.

interacts with Nedd4-2 primarily through the ligand-binding groove and surfaces of the C-terminal helix H9.

Discussion

Our cryo-EM reconstruction of full-length Nedd4-2 revealed that intramolecular interactions involving C2 domains, both HECT lobes, WW1 and WW4 mask the E2- and Ub-binding surfaces of the HECT domain (Fig. 2 and Supplementary Fig. 6b, c). Furthermore, the L region interacts with the flexible hinge that connects the two lobes of the HECT domain, thereby stabilizing its inactive conformation (Fig. 2 and Supplementary Fig. 8). This blocks access to the catalytic residue C922, which mediates Ub transfer from the E2 enzyme to the substrate[39]. To be active and able to ubiquitinate a target protein, the Nedd4-2 HECT domain must (1) be flexible around its hinge loop so that its C-lobe can move away from the N-lobe, and (2) have accessible surfaces on both lobes to accommodate the E2 enzyme and non-covalently bound Ub (Re site)[32,33,40].

When comparing the cryo-EM structure of full-length Nedd4-2 with available structures of E3 ligases of the Nedd4-family, we concluded that Nedd4-2 is autoinhibited by a multi-lock mechanism involving intramolecular interactions between structured domains, as proposed in previous structural and functional studies[17–22]. Case in point, Nedd4-2 mirrors interactions between the C-terminal section of the L region and the hinge loop observed in WWP1/2 and Itch[20–22]. However, we identified several differences between the inactive conformations of Nedd4-2 and these E3 ligases. In Nedd4-2, WW1 completely covers the Ub-binding exosite at the HECT N-lobe, due to its interaction with the groove at the interface of C2/N-lobe. This interaction also brings WW1 closer to the HECT C-lobe (Fig. 2 and Supplementary Fig. 8b–d). Conversely, in WWP1/2 and Itch, WW2 performs this masking function, as the WW domain preceding the L region, and only partly covers the Re site, but the Le site is still occupied by the WW4 domain, which further stabilizes the locked conformation of the HECT domain[22]. The N-terminal section of the Nedd4-2 L region (α1 helix) also adopts a unique conformation and does not occupy the Re site (Supplementary Figs. 8b–d, 9a). This conformation contrasts with the WWP1/2 and Itch structures, whose L region blocks the flexibility of the HECT domain by binding to both the Re site and the hinge between the N- and C-lobes (Supplementary Figs. 8, 9a).

Another unique feature of full-length Nedd4-2 detected in our cryo-EM reconstruction was the interaction between the C2 domain and the E2-binding surface of the HECT N-lobe, which is close to the Re site and the catalytic C922 (Fig. 2 and Supplementary Figs. 6b, c, 8b–d). In this conformation, the C2 domain covers the surface of helix α11 of the N-lobe with the residues that provide the E3 ligase with specificity and selectivity to E2 enzymes[32,39,41] (Fig. 2a). These results corroborate the findings of previous NMR-based studies that have mapped the C2 binding site to the N-lobe of the HECT domain[18,19] and explained why Nedd4-2 and Smurf2 activity markedly increase after removing the C2 domain[16,18,22]. The C2 domain also directly interacts with the WW1 domain through the loop between β5 and β6 (Fig. 2a).

Comparison of the full-length Nedd4-2 structure with the crystal structure of the isolated HECT domain of Smurf2[42] revealed that the N-lobe of both Nedd4-2 HECT domains adopts a similar structure in the region of the C2 binding site (Supplementary Fig. 28). However, previous NMR-based studies have mapped the C2 binding site to a different region of Smurf2 HECT N-lobe consisting of helices α3, α4, and α6[18,19]. This difference may be due to the fact that these NMR studies were performed with isolated HECT and C2 domains of Smurf2. The relative positions of the N- and C-lobes differ in the structures of the HECT domain alone and in the full-length protein, as revealed by comparing full-length Nedd4-2 with the crystal structure of the Nedd4-2 HECT domain alone (Supplementary Figs. 6b, 7). In full-length Nedd4-2, the HECT domain interacts with the C2, WW1, and WW4 domains, as well as with the L region (Figs. 1f, 2a), all of which are missing in the Smurf2 structure. Their absence may explain why the isolated Smurf2 HECT domain interacts differently with the C2 domain compared to the cryo-EM structure of full-length Nedd4-2. Therefore, our cryo-EM structure of full-length Nedd4-2 not only confirms that some members of the Nedd4 family of E3 ligases, including Smurf2, are regulated by an autoinhibitory multi-lock mechanism[16–19,43], but also highlights that the C2 domain is a key component of this mechanism. Through the C2 domain, Ca^{2+}-mediated membrane translocation markedly enhances the enzymatic activity of Nedd4-2 in vivo[14,16]. Based on this and recent structural studies, some researchers have hypothesized that Nedd4-2 is activated by blocking the inhibitory interaction between C2 and HECT[16–19,22]. Supporting this hypothesis, NMR titrations with isolated C2 and HECT domains have shown that the C2 domain of Nedd4-2 binds to Ca^{2+} (in the mM range), phospholipids, and the HECT domain using the same interface[17]. In line with these findings, our cryo-EM reconstruction revealed interactions between the C2 domain and the HECT and WW1 domains through loops containing residues involved in Ca^{2+} binding (Figs. 1f, 2a and Supplementary Fig. 9b, c). However, we were unable to capture any state of Nedd4-2 with calcium bound using cryo-EM, which is consistent with weak Ca^{2+} binding (Supplementary Figs. 6a, 11e, f). Changes in deuterium uptake at the interfaces between the C2/HECT, L/HECT, and WW4/HECT shown by HDX-MS suggest that Ca^{2+} induces transient structural fluctuations in Nedd4-2 (Fig. 3), but our cryo-EM and SAXS models indicate that these conformational changes involve only a very small fraction of Nedd4-2. These results are consistent with the low Ca^{2+}-binding affinity of the C2 domain and with the absence of changes in Nedd4-2 activity with and without 1 mM Ca^{2+} (Fig. 1e). So, while calcium alone is not able to relieve the inhibitory interaction between C2 and HECT. Ca^{2+}-induced conformational fluctuations at the interdomain interfaces may help to disrupt autoinhibitory interactions during subsequent membrane binding.

In the presence of both Ca^{2+} and BE-based LUVs, our HDX-MS measurements revealed a considerable increase in deuterium uptake in many regions of Nedd4-2, including the interfaces between C2 and HECT and between the N- and C-lobes of HECT, indicating loosening of the Nedd4-2 structure (Fig. 5). This conformational change likely results from the relaxation of the interaction between C2 and HECT following Ca^{2+}-dependent C2 membrane binding, corroborating previous models of Nedd4-2 regulation[16–19,22]. Changes in deuterium uptake were much stronger with both Ca^{2+} and LUVs (Fig. 5) than with Ca^{2+} alone (Fig. 3), so Ca^{2+}-dependent membrane binding, but not Ca^{2+} binding per se, is a critical factor in relaxing the C2/HECT interaction. Furthermore, membrane binding requires that both Ca^{2+}-binding sites of the C2 domain be intact, as removing any residue involved in Ca^{2+} coordination precluded Nedd4-2 membrane binding (Fig. 4), implying cooperative Ca^{2+} and phospholipid binding to the C2 domain. In addition, analysis of the hydrophobicity of the Nedd4-2 sequence together with HDX-MS indicated that the β1-β2 loop of the C2 domain is involved in direct membrane interactions along with other parts of Nedd4-2, including several regions of the HECT domain (Fig. 5 and Supplementary Fig. 19).

Another factor of Nedd4-2 regulation is phosphorylation-dependent 14-3-3 protein binding[25–28]. In our previous study with Nedd4-2ΔN lacking the C2 domain, we showed that 14-3-3η binding induces a conformational rearrangement of Nedd4-2[28,29]. In this study, 14-3-3 binding did not induce any significant structural changes in full-length Nedd4-2 but inhibited its membrane binding and enzymatic activity (Fig. 6c–e). Nedd4-2 interactions with BE-LUVs significantly affected the deuterium uptake of the WW2 domain (Fig. 5), suggesting changes in its interactions with other Nedd4-2 regions and/or the membrane. 14-3-3 binding to Nedd4-2 masks the C-terminal region of WW2 (residues 401–433) (Supplementary Fig. 23), which may interfere with the change in Nedd4-2 conformation and thus prevent its membrane binding and activation. Masking WW2 and WW3 may also inhibit

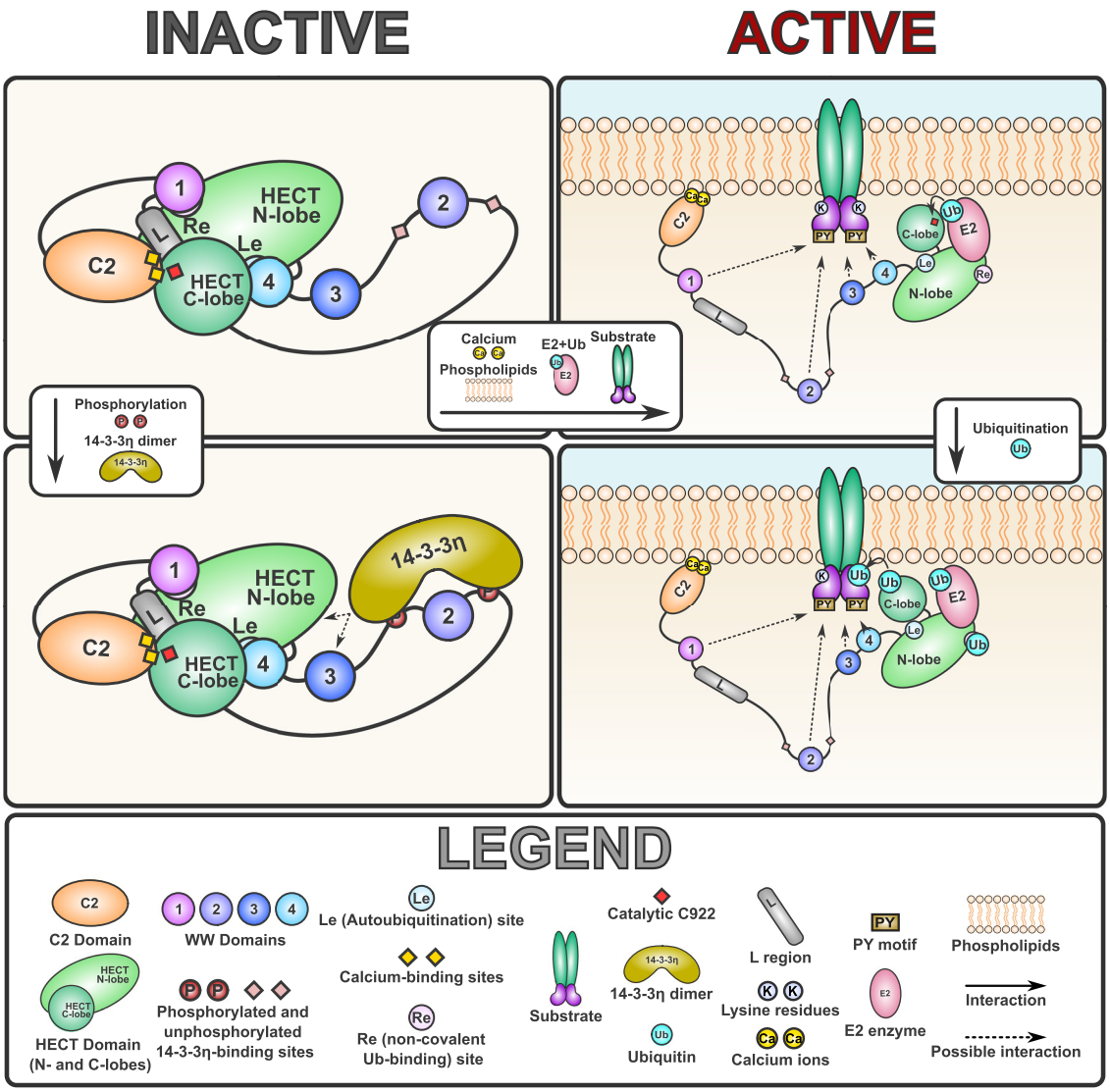

Fig. 7 | Model of Nedd4-2 regulation by autoinhibition, 14-3-3 protein, and calcium ions binding. In the inactive state, Nedd4-2 is autoinhibited by a "multi-lock" mechanism whereby the L region restricts HECT flexibility, the C2 and WW1 domains mask Ub- (re site) and E2-binding surfaces, while WW4 masks the region containing the autoubiquitination site K580 (Le site). Phosphorylation-dependent 14-3-3 protein binding to motifs adjacent to the WW2 domain blocks the WW2 and WW3 domains, thereby inhibiting Nedd4-2 membrane association and enzymatic activity. Ca^{2+}-dependent membrane binding, substrate binding (via the WW domains), and dephosphorylation of 14-3-3 binding motifs release inhibitory intra- and intermolecular interactions. Schematic illustration was created in Inkscape v1.3.

Nedd4-2 because these domains recognize substrate proteins, but we cannot rule out transient interactions between 14-3-3 and the HECT domain, as previously observed in N-terminally truncated Nedd4-2ΔN[28,29]. However, it is clear that full-length Nedd4-2 behaves differently from Nedd4-2ΔN, probably due to the C2 domain. This domain stabilizes the autoinhibited locked conformation of Nedd4-2, which 14-3-3 binding alone cannot disrupt.

In subsequent studies, the structure of the Nedd4-2/14-3-3 complex and Nedd4-2 must be solved in the presence of phospholipids to elucidate structural changes induced by 14-3-3 protein and/or membrane binding. Such studies will help us to understand how these interactions contribute to the overall process of Nedd4-2 regulation and to ascertain whether they can be targeted for treating Nedd4-2-related diseases. For now, our cryo-EM reconstruction of full-length Nedd4-2 has elucidated the structural mechanism of Nedd4-2 autoinhibition.

The C2 domain blocks the E2-binding surface of the HECT domain of Nedd4-2. This blocking, Re site masking by WW1, Le site masking by WW4, catalytic C922 blocking, and HECT domain stabilization by the L region provide the structural basis for Nedd4-2 autoinhibition (Fig. 7). The release of the C2/HECT interaction requires Ca^{2+}-dependent Nedd4-2 membrane binding via the C2 domain. However, Ca^{2+} alone is unable to disrupt the C2/HECT interaction. Phosphorylation-dependent 14-3-3 protein binding also contributes to Nedd4-2 inhibition by blocking Nedd4-2 membrane binding and further reducing its enzymatic activity.

Methods

Nedd4-2 expression, purification, and phosphorylation

Codon-optimized full-length Nedd4-2 Isoform 5 (Nedd4-2) (UniProt ID: Q96 PU5-5) subcloned into the pGEX-6P-1 GST expression vector was kindly provided by Arthur L. Haas (Louisiana State University School of Medicine, New Orleans, LA, USA)[44,45]. The PreScission Protease site in the original construct was modified to a TEV protease cleavage site using the QuikChange site-directed mutagenesis kit (Agilent, Santa Clara, CA, USA). Nedd4-2 mutants (D36L, D42L, D95L, N97L, D102L,

D103L, M122L, kinase dead C922S, C2 domain, R98A + T100A + R101A, N205A + R208A + H214A, R537A + H549A + K552A, and R98A + T100A + R101A + N205A + R208A + H214A) were created using the QuikChange kit (Agilent, Santa Clara, CA, USA) and confirmed by sequencing.

Nedd4-2 protein variants were expressed with an N-terminal GST-tag in *Escherichia coli* BL21 (DE3) cells[44,45]. Overnight cultures (5 mL) grown at 37 °C in Luria-Bertani (LB) media containing ampicillin (100 μg/mL) were transferred into 0.5 L LTB autoinduction media (0.25 L Luria-Bertani, 0.25 L Terrific broth, 0.25 g $MgSO_4 \cdot 7\ H_2O$, 2 mL glycerol, 250 mg glucose, and 1 g lactose). Cells were grown at 37 °C until 0.8 OD_{600} and then at 21 °C for 18 h. Pelleted cells were resuspended in lysis buffer (1 × PBS, 500 mM NaCl, 1 mM EDTA, 1 mM EGTA, 1 mM DTT), disrupted by freeze-thawing and sonication, and purified on a Glutathione Sepharose 4 Fast Flow column (Cytiva, Danaher Corporation, Washington, D.C., USA).

Once purified, proteins were dialyzed against a buffer (20 mM HEPES (pH 7.5), 500 mM KCl, 2 mM EDTA, 1 mM DTT, 10% (w/v) glycerol). The GST-tag was cleaved by incubation with TEV protease (250 U TEV per 1 mg fusion protein) in dialysis buffer overnight at 4 °C. The cleaved protein was then purified by size-exclusion chromatography on a HiLoad 26/600 Superdex 200 pg column (Cytiva, Danaher Corporation, Washington, D.C., USA) in buffer (20 mM HEPES (pH 7.5), 500 mM KCl, 1 mM TCEP, 10% (w/v) glycerol). Purified Nedd4-2 was phosphorylated with 170 U PKA (Promega, Madison, WI, USA) per mg protein with 0.75 mM ATP and 20 mM $MgCl_2$ and incubated at 30 °C for 2 h and then at 4 °C overnight. Excess ATP was removed by size-exclusion chromatography on a Superdex 200 Increase 10/300 GL column (Cytiva, Danaher Corporation, Washington, D.C., USA) in buffer (20 mM HEPES (pH 7.5), 150 mM NaCl, 1 mM TCEP, 10% (w/v) glycerol). The protein was then flash-frozen for subsequent use. The typical yield was 4–5 mg pure protein per 1 L LTB media.

14-3-3η protein expression and purification

14-3-3η protein was expressed in *Escherichia coli* BL21(DE3) cells using a modified pET-15b plasmid with an N-terminal His_6-tag and TEV protease site. Cells were induced with IPTG and grown overnight at 18 °C. After lysis, the protein was purified by Ni-NTA affinity chromatography followed by His_6-tag removal by TEV protease and anion-exchange chromatography on HiTrap Q (Cytiva, Danaher Corporation, Washington, D.C., USA). The final purification step was size-exclusion chromatography on a HiLoad Superdex 75 10/300 GL column (Cytiva, Danaher Corporation, Washington, D.C., USA) in buffer (20 mM Tris·HCl pH 7.5, 150 mM NaCl, 5 mM DTT, 10% glycerol)[46,47]. Purified protein was flash-frozen in liquid nitrogen and stored at −80 °C.

Uba1, Ube2d2, and Ub expression and purification

Kindly provided by Dr. Jan Silhan (IOCB, CAS), the coding sequences for mouse ubiquitin-like modifier-activating enzyme 1 (Uba1) and ubiquitin-conjugating enzyme E2D2 (Ube2d2) and human ubiquitin (Ub) were subcloned into plasmids (pET28a for Uba1 (E1) and pET-15b for Ube2d2 (E2) and Ub), each with a TEV-cleavable N-terminal 6×His-tag and expressed in *Escherichia coli* BL21 (DE3) cells grown in LB media at 16 and 25 °C, respectively, by induction at 0.8 OD_{600} for 20 h. Pelleted cells were resuspended in lysis buffer (1 × PBS, 1 M NaCl, 4 mM β-mercaptoethanol, 2 mM imidazole) and purified on a Chelating Sepharose Fast Flow column (Cytiva, Danaher Corporation, Washington, D.C., USA).

The proteins were dialyzed against a buffer (20 mM Tris-HCl (pH 7.5), 150 mM NaCl, 2 mM EDTA, 2 mM β-mercaptoethanol, 10% (w/v) glycerol). The 6×His-tag of Uba1 was cleaved by TEV protease (250 U TEV per 1 mg fusion protein) at 30 °C for 2 h, followed by dialysis overnight. Final purity was confirmed by size-exclusion chromatography on a Superdex 200 or 75 Increase 10/300 GL (Cytiva, Danaher Corporation, Washington, D.C., USA) column in buffer (20 mM Tris-HCl (pH 7.5), 150 mM NaCl, 2 mM DTT, 10% (w/v) glycerol). Proteins were concentrated as required, aliquoted, and flash-frozen in liquid nitrogen.

Human ubiquitin was labeled with fluorescein-5-maleimide (Thermo Fisher Scientific, Waltham, MA, USA; Cat. No. V49051) by incubating purified protein with a 25-fold molar excess of dye for 2 h at room temperature and then overnight at 4 °C in the dark, according to the manufacturer's instructions. Excess dye was removed by size-exclusion chromatography on a Superdex 75 Increase 10/300 GL column (Cytiva, Danaher Corporation, Washington, D.C., USA) in buffer (20 mM Tris-HCl (pH 7.5), 150 mM NaCl). Labeling was assessed by MS analysis.

ClC-5 expression, purification, and labeling

Human chloride transporter 5 (ClC-5) protein (residues 571-746, P51795-1 sequence) was expressed from pET28b+ with a C-terminal 6×His-tag (kindly provided by Dr. Raimund Dutzler, UZH, Switzerland)[48] in *Escherichia coli* BL21 (DE3) cells by isopropyl-β-D-thiogalactopyranoside (IPTG) induction (0.5 mM) at 20 °C overnight. Cells were harvested, resuspended in lysis buffer (50 mM Tris-HCl (pH 7.5), 150 mM NaCl, 5 mM $MgCl_2$, 5 mM β-mercaptoethanol), and disrupted by freeze-thawing followed by sonication.

ClC-5 was purified by Ni^{2+} affinity chromatography followed by size-exclusion chromatography on a HiLoad 26/600 Superdex 75 pg column (Cytiva, Danaher Corporation, Washington, D.C., USA) in buffer (50 mM Tris-HCl (pH 7.5), 150 mM NaCl, 5 mM $MgCl_2$, 1 mM TCEP, 10% (w/v) glycerol)[48,49].

ClC-5 was labeled with Alexa Fluor 633 NHS Ester (Succinimidyl Ester) dye (AF633, Thermo Fisher Scientific Inc., Waltham, MA, USA; Cat. No. V49090) by dialysis against buffer without amines (1×PBS (pH 7.5), 1 mM TCEP) followed by incubation with 3× molar excess AF633 at room temperature for 1 h and then overnight at 4 °C, with shaking, in the dark. Excess dye was removed by dialysis against 1×PBS buffer (pH 7.4) with 10% glycerol for 24 h and subsequently using 5 mL Zeba Spin Desalting Columns (Thermo Fisher Scientific Inc., Waltham, MA, USA). MS analysis showed 37% labeling. This protein was used as a fluorescently labelled substrate in ubiquitination assays.

Liposome-binding assay

All lipids (1-palmitoyl-2-oleoyl-*sn*-glycero-3-phosphocholine (PC/POPC), 1-palmitoyl-2-oleoyl-*sn*-glycero-3-phosphoethanolamine (PE/POPE), 1-palmitoyl-2-oleoyl-*sn*-glycero-3-phospho-L-serine (PS/POPS), cholesterol (sheep wool, 98%), 1-palmitoyl-2-oleoyl-*sn*-glycero-3-phosphoinositol (PI/POPI), and brain polar lipid extract (porcine) (BE)) were purchased from Avanti Polar Lipids Inc. (Croda International Plc, Alabaster, AL, USA) either dissolved in chloroform or as a powder (subsequently dissolved in chloroform to the desired concentration) and stored at −20 °C. They were used without further purification as described in the protocol below. We prepared four different large unilamellar vesicles (LUVs), namely a negative control (80:20 PC:PE), nuclear (61:21:4:7:7 PC:PE:PS:PI:cholesterol) and plasma (12:35:22:9:22 PC:PE:PS:PI:cholesterol) membrane-mimicking[50,51], and BE-based LUVs.

Our in vitro liposome-binding assay was based on a protocol by ref. 52. After evaporating the lipid mixture (200 nmol/sample) using the SpeedVac, we resuspended the lipids in extrusion buffer (25 mM HEPES (pH 7.5), 20% sucrose, 1 mM TCEP) for 75 min at room temperature. Each sample was sonicated for 5 s. Extrusion was performed 13 times by the Avanti Mini Extruder with 0.1-μm membranes. The resulting LUVs were then dissolved in binding buffer (25 mM HEPES (pH 7.5), 150 mM NaCl, 1 mM TCEP) and centrifuged at 18,600×*g* for 60 min at 22 °C. The supernatant was discarded, and the pellet was resuspended in 60 μL binding buffer containing 25 pmol target protein(s) (or more based on the needed molar excess) with or without 1 mM $CaCl_2$ or 1 mM EDTA. Samples were incubated for 45 min at room temperature and centrifuged at 16,000×*g* for 30 min at 22 °C. The supernatant (~50–60 μL) was collected for SDS-PAGE. The pellet was

washed with 100 µL binding buffer, transferred to a new Eppendorf tube, and recentrifuged to remove non-specifically bound proteins. The pellet was resuspended in 20 µL binding buffer and analyzed by SDS-PAGE. Band intensity was quantified by densitometry in Image Lab software v6.1.0 (Bio-Rad Laboratories, Inc., Hercules, CA, USA). Data were fitted in GraphPad Prism 10 software (Insight Partners, New York City, NY, USA).

Multi-angle dynamic light scattering (MADLS)

MADLS measurements were performed on a Zetasizer Ultra (Malvern Panalytical Ltd., Malvern, UK) with a 633 nm He–Ne laser light source and an avalanche photodiode (APD) detector. Scattering intensity was collected at 13, 90, and 173° angles and at 25 °C. Data were analyzed using the ZS XPLORER software v3.22 (Malvern Panalytical Ltd., Malvern, UK). The refractive index was set to 1.45 for liposomes before measuring 200 nmol liposomes in binding buffer with four $CaCl_2$ concentrations (0, 0.25, 0.5, and 1 mM).

Ubiquitination assays

In vitro ubiquitination assays were performed in 60 µL reaction buffer (20 mM Tris-HCl (pH 7.5), 150 mM NaCl, 5 mM $MgCl_2$, 10% glycerol) with 4 µg ubiquitin, 4 µg fluorescently labelled ubiquitin, 0.4 µg E2 (mouse Ube2d2), 0.1 µg E1 (mouse Uba1), 2 µg Nedd4-2 and with or without 2 µg fluorescently labelled ClC-5. The reaction was started by adding ATP (2 mM final concentration), followed by incubation at 22 °C. After each time point, the reaction was stopped by adding fresh SDS-PAGE loading buffer with β-mercaptoethanol and incubating at 95 °C for 2 min. Samples were resolved using SDS-PAGE 4–15% Mini-PROTEAN TGX gels (BIO-RAD) or 12% SDS-PAGE gels. All gels were scanned on a Typhoon 9500 FLA laser scanner at 473 and 635 nm (near the excitation wavelength of fluorescein-5-maleimide and Alexa Fluor™ 633 NHS Ester, respectively). The polyubiquitinated products were quantified using Image Lab software v6.1.0 (Bio-Rad Laboratories, Inc., Hercules, CA, USA) by measuring the density of bands with a molecular weight equal to or greater than that of Nedd4-2 with 1 ubiquitin molecule. Subsequently, the gels were stained with Coomassie brilliant blue and scanned using a Fusion Solo S scanner (Vilber Lourmat). Unmodified Nedd4-2 bands at different time points were quantified using Image Lab software v6.1.0 (Bio-Rad Laboratories, Inc., Hercules, CA, USA) and normalized to the zero time point (Figs. 1, 2) or the absence of 14-3-3 (Fig. 6). This quantification method monitors the disappearance of the starting material (Nedd4-2). All assays were performed on at least three independent experiments with similar results. Data were fitted using GraphPad Prism 10 software (Insight Partners, New York City, NY, USA).

Circular dichroism (CD) spectroscopy

CD spectra were measured using a 0.1 cm quartz cuvette on a ChirascanTM-plus spectrometer (Applied Photophysics, Leatherhead, Surrey, United Kingdom). Nedd4-2 wild-type and mutant variants (Nedd4-2 D36L, D42L, D95L, N97L, D102L, D103L, and M122L) were diluted in buffer to 0.2 $mg.mL^{-1}$ final concentration. The day before, proteins were dialyzed against a buffer (10 mM sodium phosphate (pH 7.4), 1 mM TCEP). Data were recorded in the 195-260 nm wavelength range with a 1 nm step and 1 s time per point at room temperature. The resulting spectra were buffer-subtracted and normalized to the concentration of the corresponding samples above and are presented as molar ellipticity vs. wavelength. Data were processed in CDNN 2.1 and BeStSel software (https://bestsel.elte.hu/index.php, ELTE Eötvös Loránd University, Budapest, Hungary).

Differential scanning fluorimetry (DSF)

DSF was performed in a real-time PCR LightCycler 480 II (Roche Applied Science, Penzberg, Germany)[53] to compare the thermal stability of Nedd4-2 wild-type and mutant variants (Nedd4-2 D36L, D42L, D95L, N97L, D102L, D103L, and M122L) at 0.2 $mg.mL^{-1}$. The total reaction volume was 25 µL. Buffer composition was 10 mM sodium phosphate (pH 7.4) and 1 mM TCEP.

Analytical ultracentrifugation (AUC)

Full-length Nedd4-2 and 14-3-3η were dialyzed against buffer (20 mM HEPES (pH 7.5), 150 mM NaCl, 1 mM TCEP, 1 mM EDTA (or 1 mM $CaCl_2$, where indicated)) and loaded into double-sector titanium centerpieces with 12 mm optical path length (Nanolytics Instruments, Potsdam, Germany). Sedimentation velocity (SV) experiments were performed on a ProteomLab XL-I analytical ultracentrifuge (Beckman Coulter, Brea, CA, USA) at 20 °C and 40,000 rpm rotor speed (An-50 Ti rotor, Beckman Coulter), and sedimentation profiles were acquired by measuring absorbance at 280 nm. Buffer parameters were estimated using SEDNTERP v3.0.4[54]. The $c(s)$ of 0.5 µM Nedd4-2 and 0.1–10 µM 14-3-3η mixtures were calculated from raw data using SEDFIT v17.0 and further integrated to determine $s_{w(20,w)}$[55,56]. s_w values were plotted as a function of 14-3-3η concentration to construct s_w isotherms, which were fitted with an $A + B \rightleftharpoons AB$ model, as implemented in the SEDPHAT v15.2c software package, with previously known s_w values of each component. The parameters were verified, and the loading concentrations were corrected by global Lamm equation modeling in SEDPHAT v15.2c software[57].

Cryo-EM - sample preparation and data collection

To prepare grids, thawed Nedd4-2 was purified by size-exclusion chromatography on a Superdex 200 10/300 GL column (GE Healthcare, Chicago, IL, USA) in buffer (20 mM HEPES (pH 7.5), 130 mM KCl, 20 mM NaCl, 1 mM EDTA, and 1 mM TCEP). Peak fractions were diluted twofold in buffer (20 mM HEPES (pH 7.5), 130 mM KCl, 20 mM NaCl, 1 mM EDTA, 1 mM TCEP, 6 mM CHAPSO) to final concentrations of 3 mM CHAPSO and 2.7 $mg.mL^{-1}$ protein (without Ca^{2+}) or 3.4 $mg.mL^{-1}$ (with Ca^{2+}). In the case of Nedd4-2 with calcium, 1 mM EDTA was replaced by 1 mM $CaCl_2$. Subsequently, 3.5 µL protein solution was applied to freshly glow-discharged (45 s total time, Gatan Solarus II 955 (Gatan, Inc., Pleasanton, CA, USA)) UltrAuFoil holey grids (R1.2/1.3, Quantifoil, Großlöbichau, Germany) and blotted on a Vitrobot Mark IV system for 4 s at 20 °C and 100% humidity. All grids were plunge-frozen in liquid ethane and stored in liquid nitrogen before screening under a JEOL JEM 2100-plus electron microscope (Akishima, Tokyo, Japan) at 200 keV equipped with a TVIPS TemCam–XF416 4 K CMOS camera (TVIPS GmbH, Gauting, Germany) and under a Talos Arctica electron microscope (FEI, Thermo Fisher Scientific, Hillsboro, Oregon, USA) at 200 keV equipped with a GATAN K2 Summit detector (Gatan, Inc., Pleasanton, CA, USA). All data were collected under a Titan Krios electron microscope (FEI, Thermo Fisher Scientific, Hillsboro, Oregon, USA) at 300 keV equipped with a Gatan K3 BioQuantum detector (Gatan, Inc., Pleasanton, CA, USA). All 40-frame movies were recorded at 105,000× magnification and 0.834 Å calibrated pixel size, with defocus values ranging from −0.7 to −2.8 µm and 40 $e^-/Å^2$ total exposure.

Cryo-EM image processing

All cryo-EM images were processed in CryoSPARC 4.4.1[58]. Once the movies were imported, gain correction and patch motion correction was followed by patch CTF estimation. Micrographs with estimated CTF resolution >5 Å, full-frame motion distance >20 Å, and relative ice thickness >1.2 were discarded; then, micrographs were visually curated, removing those with excessive aggregation or ice or power spectrum artifacts. From 200 randomly selected micrographs, the initial particle set was picked using a blob picker (100–200 Å particle size). After visual inspection, particles were extracted with a 300 × 300 pixel box size, followed by 2D classification to generate templates from good classes. Particle picking was repeated with a template-based picker, selected particles were extracted with a box size of 380 × 380

pixels, followed by 2D classification. Particles in good 2D classes were used for ab initio 3D reconstruction (300/1000 initial/final minibatch size parameters), heterogeneous refinement (default settings), and homogeneous (default settings), non-uniform (initial lowpass resolution set to 20 Å, with a maximum align resolution of 3 Å) and local refinements (activated pose/shift gaussian prior) according to the supplemental workflow scheme (Supplementary Figs. 3, 4). Particles in the 3D class of Nedd4-2 were reference-based motion corrected in CryoSPARC 4.4.1[59]. The final map resolution was determined by gold-standard FSC calculation with a 0.143 FSC threshold and sharpened with phenix.autosharpen (Phenix 1.19.1)[60]. Details on data collection, processing, and validation are listed in Supplementary Table 1.

Cryo-EM - model building, refinement, and analysis

After visual inspection of the final map, known crystal structures of Nedd4-2 domains, namely C2 (PDB: 2NSQ) and HECT (PDB: 2ONI), were fitted using the "jiggle-fit" tool in Coot 0.9.8[61]. Missing regions were modeled with Modelangelo[62] and manually adjusted and corrected, excluding areas with insufficient or uninterpretable density. Atomic refinement with phenix.real_space_refine in the software package Phenix 1.19.1[60] preceded model validation with MolProbity[63]. Model statistics are presented in Supplementary Table 1 and Supplementary Figs. 3, 4. The final models are deposited in PDB/EMDB under accession codes 9GIK/51373 and 9GIM/51374.

Hydrogen-deuterium exchange coupled to mass spectrometry (HDX-MS)

Nedd4-2 (10 μM), 14-3-3η (20 μM), their 1:2 complex, with and without 1 mM Ca^{2+}, and 10 μM Nedd4-2 with 1 mM $CaCl_2$ and LUVs (200 nmol LUVs per 500 pmol Nedd4-2) were preincubated for 30 min at 4 °C (45 min for samples with LUVs) and subjected to H/D exchange. HDX reactions were initiated by diluting the protein mixture 10× in a D_2O-based buffer (20 mM HEPES (pD 7.5), 150 mM KCl, 1 mM TCEP, and 1 mM $CaCl_2$ (or 1 mM EDTA). Both buffer and protein solution were pre-equilibrated for 1 h at the temperature of the subsequent HDX experiment (20 °C). HDX kinetics were sampled for 20 s, 2 min, 20 min, and 2 h incubation with deuterons at 20 °C. Three independently generated exchange reactions (technical replicates, $n = 3$) were performed for 20-s and 20-min reactions. The samples were quenched by adding 100 μl chilled quench buffer (6 M urea, 2 M thiourea, 400 mM TCEP, 1 M glycine-HCl (pH 2.3)) in a 1:1 ratio, manually injected into the temperature-controlled LC system of a PAL DHR autosampler (CTC Analytics AG, Zwingen, Switzerland), controlled by Chronos software (Axel Semrau GmbH & Co, Trajan Scientific and Medical, Melbourne, Australia). Samples without LUVs were applied to a custom-made pepsin/nepenthesin-2 protease column, while samples with LUVs were processed on a column packed with immobilized pepsin and AnPep coupled in tandem with a nepenthesin-2 protease column (bed volume 66 μL, AffiPro) under a flow of 0.4% formic acid (FA) in water at 200 μL.min^{-1} flow rate (1260 Infinity II Quaternary pump, Agilent Technologies, Waldbronn, Germany).

The resulting peptides were trapped online, desalted on a SecurityGuard™ precolumn (ULTRA Cartridges UHPLC Fully Porous Polar C18, 2.1 mm, Phenomenex, Torrance, CA, USA) for 3 min and then separated on a reversed-phase analytical column (LUNA® Omega Polar C18 Column, 100 Å, 1.6 μm, 100 mm × 1.0 mm, Phenomenex, Torrance, CA, USA) at 40 μL.min^{-1} flow rate using a 10–40% linear gradient of solvent B (A: 2% acetonitrile/0.1% FA in water; B: 98% acetonitrile/0.1% FA in water) (1290 Infinity II LC system, Agilent Technologies, Waldbronn, Germany). The LC system was interfaced with the ESI source of a TimsTOF Pro mass spectrometer (Bruker Corporation, Billerica, MA, USA) at 0 °C to minimize back-exchange. For deuterium back-exchange correction, fully deuterated control samples were prepared (n = 3) using the same LC setup in offline mode. Desalted peptides were captured, dried, redissolved in D_2O-based buffer (pD 7.5) incubated overnight at 37 °C and analyzed using the same setup.

The mass spectrometer was operated in MS mode with 1 Hz data acquisition. LC-MS data were peak picked and exported in DataAnalysis software (v. 5.3, Bruker Daltonics), further processed in DeutEx software[64], and presented in the MS Tools platform (http://peterslab.org/MSTools/)[65]. Peptides were identified in the same LC-MS system, albeit with the mass spectrometer operating in data-dependent MS/MS mode using PASEF. LC-MS/MS data were searched using MASCOT (v. 2.7, Matrix Science) against a customized database combining Nedd4-2, 14-3-3η, common cRAP.fasta (https://www.thegpm.org/crap/) and protease sequences, setting the following search parameters: no enzyme, Ser, Thr, or Tyr phosphorylation allowed as variable post-translational modification, 10 ppm precursor tolerance, 0.05 Da fragment ion tolerance, decoy search enabled, FDR ˂1%, IonScore ˃20, and peptide length ˃5.

The HDX data summary table and the HDX data table are included in Supplementary Data 1, 2 as per consensus guidelines[66]. The mass spectrometry data have been deposited in the ProteomeXchange Consortium (http://proteomecentral.proteomexchange.org) via the PRIDE partner repository[67] with the dataset identifier PXD058899.

Small-angle X-ray scattering (SAXS)

Synchrotron SAXS data were collected at P12 BioSAXS beamline operated by EMBL Hamburg at the PETRA III storage ring (Deutsches Elektronen-Synchrotron (DESY), Hamburg, Germany). SEC-SAXS measurements were conducted using a Superdex 200 Increase 5/150 GL column (Cytiva, Danaher Corporation, Washington, D.C., USA) in buffer (20 mM HEPES (pH 7.5), 150 mM NaCl, 1 mM TCEP, 3% (w/v) glycerol) at 0.3 mL.min^{-1} flow rate and 293.15 K. For measurements with calcium, an additional 1 mM $CaCl_2$ was included in both the sample and SEC mobile phase. For measurements without calcium, both the sample and SEC mobile phase contained 1 mM EDTA. Further details are outlined in Supplementary Table 2. SEC-SAXS elution profiles were processed using the program CHROMIXS within the ATSAS package v3.2.1[68]. Data range selection was based on constant R_g where possible. The scattering profiles were used to determine the molecular mass, Porod volume, and R_g in PRIMUS within the ATSAS package v3.2.1[69]. The pair-distance distribution function *P(r)* was calculated using the program GNOM within the ATSAS package v3.2.1[70].

SAXS-based modeling

Solution structure modeling of Nedd4-2 from SAXS data was done with the program CORAL within the ATSAS package v3.0.1[36]. The cryo-EM structure of Nedd4-2 (this work), the crystal structure of the WW3 domain (PDB ID: 1wr7)[71], and the AlphaFold2[72] derived structure of the WW2 domain with flanking linkers were used as input structures. The best-scoring CORAL model was chosen according to the lowest χ^2. A low-resolution electron density map was calculated using DENSS v1.6[73]. An averaged map was constructed from 50 runs with the denss.all.py script, which was further refined with the denss.refine.py script.

Statistics and reproducibility

Liposome-binding and ubiquitination results (Figs. 1, 2, 4, 6) are expressed as means ± S.D. from three replicates, as indicated in figure legends. Statistical tests were performed in GraphPad Prism 10 (Insight Partners, New York City, New York). Significant differences from the control were determined using an unpaired two-tailed Student's *t*-test, as stated in figure legends (ns non-significant $p > 0.05$; *$p \le 0.05$; **$p \le 0.01$; ***$p \le 0.001$; ****$p \le 0.0001$) (Figs. 1c, d, 2b, 4a, b, d, 6c–e and Supplementary Figs. 10b, 15a, b, 22a–c).

Reporting summary

Further information on research design is available in the Nature Portfolio Reporting Summary linked to this article.

Data availability

The authors declare that all data supporting the findings of this study are available in the main text and its supplementary information files. The final cryo-EM maps and corresponding atomic coordinates generated in this study have been deposited in the Electron Microscopy Data Bank (EMDB) and the Protein Data Bank (PDB) under the accession codes EMD-51373, 9GIK (Nedd4-2) and EMD-51374, 9GIM (Nedd4-2 + Ca^{2+}). HDX data summary table is available in Supplementary Data 1 and the HDX data table are available as Supplementary Data 2. The mass spectrometry proteomics data have been deposited in the ProteomeXchange Consortium (http://proteomecentral.proteomexchange.org) via the PRIDE partner repository with the dataset identifier PXD058899. The SAXS data are available in the Small-Angle Scattering Biological Data Bank (SASBDB) under accession codes SASDUC3 (Nedd4-2) and SASDUD3 (Nedd4-2 + Ca^{2+}). All datasets are freely accessible through the respective repositories. Further information may be requested from the corresponding authors. Source data are provided with this paper.

References

1. Popovic, D., Vucic, D. & Dikic, I. Ubiquitination in disease pathogenesis and treatment. *Nat. Med.* **20**, 1242–1253 (2014).
2. Foot, N., Henshall, T. & Kumar, S. Ubiquitination and the regulation of membrane proteins. *Physiol. Rev.* **97**, 253–281 (2017).
3. Rotin, D. & Kumar, S. Physiological functions of the HECT family of ubiquitin ligases. *Nat. Rev. Mol. Cell Biol.* **10**, 398–409 (2009).
4. Li, W. et al. Genome-wide and functional annotation of human E3 ubiquitin ligases identifies MULAN, a mitochondrial E3 that regulates the organelle's dynamics and signaling. *PLoS ONE* **3**, e1487 (2008).
5. Zheng, N. & Shabek, N. Ubiquitin ligases: structure, function, and regulation. *Annu. Rev. Biochem.* **86**, 129–157 (2017).
6. Harvey, K. F. & Kumar, S. Nedd4-like proteins: an emerging family of ubiquitin-protein ligases implicated in diverse cellular functions. *Trends Cell Biol.* **9**, 166–169 (1999).
7. Staub, O. et al. WW domains of Nedd4 bind to the proline-rich PY motifs in the epithelial Na^+ channel deleted in Liddle's syndrome. *EMBO J.* **15**, 2371–2380 (1996).
8. Goel, P., Manning, J. A. & Kumar, S. NEDD4-2 (NEDD4L): the ubiquitin ligase for multiple membrane proteins. *Gene* **557**, 1–10 (2015).
9. Bernassola, F., Chillemi, G. & Melino, G. HECT-Type E3 Ubiquitin ligases in cancer. *Trends Biochem. Sci.* **44**, 1057–1075 (2019).
10. Rizzo, F. & Staub, O. NEDD4-2 and salt-sensitive hypertension. *Curr. Opin. Nephrol. Hypertens.* **24**, 111–116 (2015).
11. Vanli-Yavuz, E. N. et al. Investigation of the possible association of NEDD4-2 (NEDD4L) gene with idiopathic photosensitive epilepsy. *Acta Neurol. Belg.* **115**, 241–245 (2015).
12. Mund, T., Lewis, M. J., Maslen, S. & Pelham, H. R. Peptide and small molecule inhibitors of HECT-type ubiquitin ligases. *Proc. Natl Acad. Sci. USA* **111**, 16736–16741 (2014).
13. Sudol, M. Structure and function of the WW domain. *Prog. Biophys. Mol. Biol.* **65**, 113–132 (1996).
14. Plant, P. J., Yeger, H., Staub, O., Howard, P. & Rotin, D. The C2 domain of the ubiquitin protein ligase Nedd4 mediates Ca^{2+}-dependent plasma membrane localization. *J. Biol. Chem.* **272**, 32329–32336 (1997).
15. Kim, H. C. & Huibregtse, J. M. Polyubiquitination by HECT E3s and the determinants of chain type specificity. *Mol. Cell Biol.* **29**, 3307–3318 (2009).
16. Wang, J. et al. Calcium activates Nedd4 E3 ubiquitin ligases by releasing the C2 domain-mediated auto-inhibition. *J. Biol. Chem.* **285**, 12279–12288 (2010).
17. Escobedo, A. et al. Structural basis of the activation and degradation mechanisms of the E3 ubiquitin ligase Nedd4L. *Structure* **22**, 1446–1457 (2014).
18. Wiesner, S. et al. Autoinhibition of the HECT-type ubiquitin ligase Smurf2 through its C2 domain. *Cell* **130**, 651–662 (2007).
19. Mari, S. et al. Structural and functional framework for the autoinhibition of Nedd4-family ubiquitin ligases. *Structure* **22**, 1639–1649 (2014).
20. Chen, Z. et al. A tunable brake for HECT ubiquitin ligases. *Mol. Cell* **66**, 345–357 e346 (2017).
21. Zhu, K. et al. Allosteric auto-inhibition and activation of the Nedd4 family E3 ligase Itch. *EMBO Rep.* **18**, 1618–1630 (2017).
22. Wang, Z. et al. A multi-lock inhibitory mechanism for fine-tuning enzyme activities of the HECT family E3 ligases. *Nat. Commun.* **10**, 3162 (2019).
23. Maspero, E. et al. Structure of the HECT:ubiquitin complex and its role in ubiquitin chain elongation. *EMBO Rep.* **12**, 342–349 (2011).
24. Maspero, E. et al. Structure of a ubiquitin-loaded HECT ligase reveals the molecular basis for catalytic priming. *Nat. Struct. Mol. Biol.* **20**, 696–701 (2013).
25. Bhalla, V. et al. Serum- and glucocorticoid-regulated kinase 1 regulates ubiquitin ligase neural precursor cell-expressed, developmentally down-regulated protein 4-2 by inducing interaction with 14-3-3. *Mol. Endocrinol.* **19**, 3073–3084 (2005).
26. Ichimura, T. et al. 14-3-3 proteins modulate the expression of epithelial Na^+ channels by phosphorylation-dependent interaction with Nedd4-2 ubiquitin ligase. *J. Biol. Chem.* **280**, 13187–13194 (2005).
27. Chandran, S. et al. Neural precursor cell-expressed developmentally down-regulated protein 4-2 (Nedd4-2) regulation by 14-3-3 protein binding at canonical serum and glucocorticoid kinase 1 (SGK1) phosphorylation sites. *J. Biol. Chem.* **286**, 37830–37840 (2011).
28. Pohl, P., Joshi, R., Petrvalska, O., Obsil, T. & Obsilova, V. 14-3-3-protein regulates Nedd4-2 by modulating interactions between HECT and WW domains. *Commun. Biol.* **4**, 899 (2021).
29. Joshi, R. et al. Nedd4-2 binding to 14-3-3 modulates the accessibility of its catalytic site and WW domains. *Biophys. J.* **121**, 1299–1311 (2022).
30. Ishikawa, K. et al. Prediction of the coding sequences of unidentified human genes. VIII. 78 new cDNA clones from brain which code for large proteins in vitro. *DNA Res.* **4**, 307–313 (1997).
31. Fotia, A. B. et al. The role of individual Nedd4-2 (KIAA0439) WW domains in binding and regulating epithelial sodium channels. *FASEB J.* **17**, 70–72 (2003).
32. Kamadurai, H. B. et al. Insights into ubiquitin transfer cascades from a structure of a UbcH5B approximately ubiquitin-HECT(NEDD4L) complex. *Mol. Cell* **36**, 1095–1102 (2009).
33. French, M. E., Kretzmann, B. R. & Hicke, L. Regulation of the RSP5 ubiquitin ligase by an intrinsic ubiquitin-binding site. *J. Biol. Chem.* **284**, 12071–12079 (2009).
34. Zhang, W. et al. System-wide modulation of HECT E3 ligases with selective ubiquitin variant probes. *Mol. Cell* **62**, 121–136 (2016).
35. Nalefski, E. A. & Falke, J. J. The C2 domain calcium-binding motif: structural and functional diversity. *Protein Sci.* **5**, 2375–2390 (1996).
36. Petoukhov, M. V. et al. New developments in the ATSAS program package for small-angle scattering data analysis. *J. Appl. Crystallogr.* **45**, 342–350 (2012).
37. Kyte, J. & Doolittle, R. F. A simple method for displaying the hydropathic character of a protein. *J. Mol. Biol.* **157**, 105–132 (1982).
38. Obsilova, V. & Obsil, T. Structural insights into the functional roles of 14-3-3 proteins. *Front. Mol. Biosci.* **9**, 1016071 (2022).
39. Huang, L. et al. Structure of an E6AP-UbcH7 complex: insights into ubiquitination by the E2-E3 enzyme cascade. *Science* **286**, 1321–1326 (1999).
40. Verdecia, M. A. et al. Conformational flexibility underlies ubiquitin ligation mediated by the WWP1 HECT domain E3 ligase. *Mol. Cell* **11**, 249–259 (2003).

41. Eletr, Z. M. & Kuhlman, B. Sequence determinants of E2-E6AP binding affinity and specificity. *J. Mol. Biol.* **369**, 419–428 (2007).
42. Ogunjimi, A. A. et al. Regulation of Smurf2 ubiquitin ligase activity by anchoring the E2 to the HECT domain. *Mol. Cell* **19**, 297–308 (2005).
43. Persaud, A. et al. Tyrosine phosphorylation of NEDD4 activates its ubiquitin ligase activity. *Sci. Signal* **7**, ra95 (2014).
44. Todaro, D. R., Augustus-Wallace, A. C., Klein, J. M. & Haas, A. L. The mechanism of neural precursor cell expressed developmentally down-regulated 4-2 (Nedd4-2)/NEDD4L-catalyzed polyubiquitin chain assembly. *J. Biol. Chem.* **292**, 19521–19536 (2017).
45. Todaro, D. R., Augustus-Wallace, A. C., Klein, J. M. & Haas, A. L. Oligomerization of the HECT ubiquitin ligase NEDD4-2/NEDD4L is essential for polyubiquitin chain assembly. *J. Biol. Chem.* **293**, 18192–18206 (2018).
46. Obsil, T., Ghirlando, R., Klein, D. C., Ganguly, S. & Dyda, F. Crystal structure of the 14-3-3zeta:serotonin N-acetyltransferase complex. a role for scaffolding in enzyme regulation. *Cell* **105**, 257–267 (2001).
47. Obsilova, V. et al. 14-3-3zeta C-terminal stretch changes its conformation upon ligand binding and phosphorylation at Thr232. *J. Biol. Chem.* **279**, 4531–4540 (2004).
48. Meyer, S., Savaresi, S., Forster, I. C. & Dutzler, R. Nucleotide recognition by the cytoplasmic domain of the human chloride transporter ClC-5. *Nat. Struct. Mol. Biol.* **14**, 60–67 (2007).
49. Wellhauser, L. et al. Nucleotides bind to the C-terminus of ClC-5. *Biochem. J.* **398**, 289–294 (2006).
50. Das, S., Dixon, J. E. & Cho, W. Membrane-binding and activation mechanism of PTEN. *Proc. Natl Acad. Sci. USA* **100**, 7491–7496 (2003).
51. Ansell, G. B. *Form and Function of Phospholipids* (Elsevier Scientific Pub. Co., 1973).
52. Julkowska, M. M., Rankenberg, J. M. & Testerink, C. Liposome-binding assays to assess specificity and affinity of phospholipid-protein interactions. *Methods Mol. Biol.* **1009**, 261–271 (2013).
53. Niesen, F. H., Berglund, H. & Vedadi, M. The use of differential scanning fluorimetry to detect ligand interactions that promote protein stability. *Nat. Protoc.* **2**, 2212–2221 (2007).
54. Laue, T. M., Shah, B. D., Ridgeway, T. M. & Pelletier, S. L. in *Analytical Ultracentrifugation in Biochemistry and Polymer Science* (eds Harding, S. E., Rowe, A. J. & Horton, J. C.) (Royal Society of Chemistry, 1992).
55. Brautigam, C. A. Calculations and publication-quality illustrations for analytical ultracentrifugation data. *Methods Enzymol.* **562**, 109–133 (2015).
56. Schuck, P. Size-distribution analysis of macromolecules by sedimentation velocity ultracentrifugation and lamm equation modeling. *Biophys. J.* **78**, 1606–1619 (2000).
57. Dam, J., Velikovsky, C. A., Mariuzza, R. A., Urbanke, C. & Schuck, P. Sedimentation velocity analysis of heterogeneous protein-protein interactions: Lamm equation modeling and sedimentation coefficient distributions c(s). *Biophys. J.* **89**, 619–634 (2005).
58. Punjani, A., Rubinstein, J. L., Fleet, D. J. & Brubaker, M. A. cryoSPARC: algorithms for rapid unsupervised cryo-EM structure determination. *Nat. Methods* **14**, 290–296 (2017).
59. Zivanov, J., Nakane, T. & Scheres, S. H. W. A Bayesian approach to beam-induced motion correction in cryo-EM single-particle analysis. *IUCrJ* **6**, 5–17 (2019).
60. Liebschner, D. et al. Macromolecular structure determination using X-rays, neutrons and electrons: recent developments in Phenix. *Acta Crystallogr. D. Struct. Biol.* **75**, 861–877 (2019).
61. Emsley, P. & Cowtan, K. Coot: model-building tools for molecular graphics. *Acta Crystallogr. D. Biol. Crystallogr.* **60**, 2126–2132 (2004).
62. Jamali, K. et al. Automated model building and protein identification in cryo-EM maps. *Nature* **628**, 450–457 (2024).
63. Williams, C. J. et al. MolProbity: more and better reference data for improved all-atom structure validation. *Protein Sci.* **27**, 293–315 (2018).
64. Trcka, F. et al. Human stress-inducible Hsp70 has a high propensity to form ATP-dependent antiparallel dimers that are differentially regulated by cochaperone binding. *Mol. Cell Proteom.* **18**, 320–337 (2019).
65. Kavan, D. & Man, P. MSTools-web based application for visualization and presentation of HXMS data. *Int. J. Mass Spectrom.* **302**, 53–58 (2011).
66. Masson, G. R. et al. Recommendations for performing, interpreting and reporting hydrogen deuterium exchange mass spectrometry (HDX-MS) experiments. *Nat. Methods* **16**, 595–602 (2019).
67. Perez-Riverol, Y. et al. The PRIDE database resources in 2022: a hub for mass spectrometry-based proteomics evidences. *Nucleic Acids Res.* **50**, D543–D552 (2022).
68. Panjkovich, A. & Svergun, D. I. CHROMIXS: automatic and interactive analysis of chromatography-coupled small-angle X-ray scattering data. *Bioinformatics* **34**, 1944–1946 (2018).
69. Konarev, P. V., Volkov, V. V., Sokolova, A. V., Koch, M. H. J. & Svergun, D. I. PRIMUS: a Windows PC-based system for small-angle scattering data analysis. *J. Appl. Crystallogr.* **36**, 1277–1282 (2003).
70. Svergun, D. I. Determination of the regularization parameter in indirect-transform methods using perceptual criteria. *J. Appl. Crystallogr.* **25**, 495–503 (1992).
71. Yang, X. et al. Structural basis for protein-protein interactions in the 14-3-3 protein family. *Proc. Natl Acad. Sci. USA* **103**, 17237–17242 (2006).
72. Jumper, J. et al. Highly accurate protein structure prediction with AlphaFold. *Nature* **596**, 583–589 (2021).
73. Grant, T. D. Ab initio electron density determination directly from solution scattering data. *Nat. Methods* **15**, 191–193 (2018).

Acknowledgements

This study was funded by the Czech Science Foundation (grant 23-04686S to V.O.), the Czech Academy of Sciences (RVO: 67985823 of the Institute of Physiology), and the Visegrad Scholarship (ID: 52310440 to M.J.). We acknowledge CF CEITEC/Brno - Cryo-electron microscopy and tomography of CIISB, Instruct-CZ Centre, supported by MEYS CR (LM2023042) and European Regional Development Fund-Project "Innovation of Czech Infrastructure for Integrative Structural Biology" (No. CZ.02.01.01/00/23_015/0008175). We acknowledge CMS-Biocev ("Biophysical techniques, Crystallization, Diffraction, Structural mass spectrometry") of CIISB, Instruct-CZ Centre, supported by MEYS CR (LM2023042) and CZ.02.1.01/0.0/0.0/18_046/0015974, and Imaging Methods Core Facility at BIOCEV, supported by the MEYS CR (LM2023050 Czech-BioImaging). We thank SAXS beamline P12 (Petra III DESY, Hamburg) for the allocated experimental beam time. Computational resources were provided by the e-INFRA CZ project (ID:90254), supported by the Ministry of Education, Youth and Sports of the Czech Republic. We thank Dr. Arthur L. Haas for providing the optimized Nedd4-2 isoform 5 construct. We also thank Dana Kalabova and Gabriela Kocarova for technical assistance, Matyas Pinkas and Jiri Novacek for their help with cryo-EM measurements, Petr Pompach, Pavla Vankova, and Jan Rasl for their help with MS measurements, and Carlos V. Melo for editing the manuscript.

Author contributions

V.O. and T.O. supervised the project and provided scientific guidance. M.J., R.J., P.P., and A.T. performed protein expression and purification experiments. M.J. performed liposome binding and ubiquitination assays, statistical analysis, MADLS, DSF, and CD spectroscopy

measurements, prepared samples for cryo-EM and SAXS, designed all figures related to these assays, MADLS, DSF, and CD, and performed statistical analysis. M.J. and R.J. prepared samples for HDX-MS experiments. D.K. collected, analyzed, and processed cryo-EM data, built and refined atomic models, prepared cryo-EM-related figures, and curated and deposited structural data. A.T. performed SAXS data analysis and SAXS-based modeling and prepared HDX-MS- and SAXS-related figures and tables. K.H. performed SV-AUC measurements, analyzed data, and prepared AUC-related figures. V.O., T.O., M.J., D.K., and A.T. wrote the manuscript. All co-authors revised the manuscript.

Competing interests
The authors declare no competing interests.

Additional information
Supplementary information The online version contains supplementary material available at https://doi.org/10.1038/s41467-025-60207-4.

Correspondence and requests for materials should be addressed to Tomas Obsil or Veronika Obsilova.

Peer review information *Nature Communications* thanks Simona Polo and the other, anonymous, reviewer(s) for their contribution to the peer review of this work. A peer review file is available.